


RESEARCH ARTICLE

Open Access



# Diabetic phenotype in mouse and humans reduces the number of microglia around $\beta$ -amyloid plaques

Teemu Natunen<sup>1†</sup>, Henna Martiskainen<sup>1†</sup>, Mikael Marttinen<sup>1†</sup>, Sami Gabbouj<sup>1</sup>, Hennariikka Koivisto<sup>2</sup>, Susanna Kemppainen<sup>1</sup>, Satu Kaipainen<sup>2</sup>, Mari Takalo<sup>1</sup>, Helena Svobodová<sup>3</sup>, Luukas Leppänen<sup>1</sup>, Benjam Kemiläinen<sup>4</sup>, Simo Ryhänen<sup>1</sup>, Teemu Kuulasmaa<sup>1</sup>, Eija Rahunen<sup>1</sup>, Sisko Juutinen<sup>1</sup>, Petra Mäkinen<sup>1</sup>, Pasi Miettinen<sup>2</sup>, Tuomas Rauramaa<sup>5</sup>, Jussi Pihlajamäki<sup>6</sup>, Annakaisa Haapasalo<sup>2</sup>, Ville Leinonen<sup>4</sup>, Heikki Tanila<sup>2†</sup> and Mikko Hiltunen<sup>1\*†</sup> 

## Abstract

**Background:** Alzheimer's disease (AD) is the most common neurodegenerative disease and type 2 diabetes (T2D) plays an important role in conferring the risk for AD. Although AD and T2D share common features, the common molecular mechanisms underlying these two diseases remain elusive.

**Methods:** Mice with different AD- and/or tauopathy-linked genetic backgrounds (APPswe/PS1dE9, Tau P301L and APPswe/PS1dE9/Tau P301L) were fed for 6 months with standard diet or typical Western diet (TWD). After behavioral and metabolic assessments of the mice, the effects of TWD on global gene expression as well as dystrophic neurite and microglia pathology were elucidated. Consequently, mechanistic aspects related to autophagy, cell survival, phagocytic uptake as well as Trem2/Dap12 signaling pathway, were assessed in microglia upon modulation of PI3K-Akt signaling. To evaluate whether the mouse model-derived results translate to human patients, the effects of diabetic phenotype on microglial pathology were assessed in cortical biopsies of idiopathic normal pressure hydrocephalus (iNPH) patients encompassing  $\beta$ -amyloid pathology.

**Results:** TWD led to obesity and diabetic phenotype in all mice regardless of the genetic background. TWD also exacerbated memory and learning impairment in APPswe/PS1dE9 and Tau P301L mice. Gene co-expression network analysis revealed impaired microglial responses to AD-related pathologies in APPswe/PS1dE9 and APPswe/PS1dE9/Tau P301L mice upon TWD, pointing specifically towards aberrant microglial functionality due to altered downstream signaling of Trem2 and PI3K-Akt. Accordingly, fewer microglia, which did not show morphological changes, and increased number of dystrophic neurites around  $\beta$ -amyloid plaques were discovered in the hippocampus of TWD mice. Mechanistic studies in mouse microglia revealed that interference of PI3K-Akt signaling significantly decreased phagocytic uptake and proinflammatory response. Moreover, increased activity of Syk-kinase  
(Continued on next page)

\* Correspondence: [mikko.hiltunen@uef.fi](mailto:mikko.hiltunen@uef.fi)

<sup>†</sup>Teemu Natunen, Henna Martiskainen, Mikael Marttinen, Heikki Tanila and Mikko Hiltunen contributed equally to this work.

<sup>1</sup>Institute of Biomedicine, University of Eastern Finland, P.O. Box 1627, FI-70211 Kuopio, Finland

Full list of author information is available at the end of the article



© The Author(s). 2020 **Open Access** This article is licensed under a Creative Commons Attribution 4.0 International License, which permits use, sharing, adaptation, distribution and reproduction in any medium or format, as long as you give appropriate credit to the original author(s) and the source, provide a link to the Creative Commons licence, and indicate if changes were made. The images or other third party material in this article are included in the article's Creative Commons licence, unless indicated otherwise in a credit line to the material. If material is not included in the article's Creative Commons licence and your intended use is not permitted by statutory regulation or exceeds the permitted use, you will need to obtain permission directly from the copyright holder. To view a copy of this licence, visit <http://creativecommons.org/licenses/by/4.0/>. The Creative Commons Public Domain Dedication waiver (<http://creativecommons.org/publicdomain/zero/1.0/>) applies to the data made available in this article, unless otherwise stated in a credit line to the data.

(Continued from previous page)

upon ligand-induced activation of Trem2/Dap12 signaling was detected. Finally, characterization of microglial pathology in cortical biopsies of iNPH patients revealed a significant decrease in the number of microglia per  $\beta$ -amyloid plaque in obese individuals with concomitant T2D as compared to both normal weight and obese individuals without T2D.

**Conclusions:** Collectively, these results suggest that diabetic phenotype in mice and humans mechanistically associates with abnormally reduced microglial responses to  $\beta$ -amyloid pathology and further suggest that AD and T2D share overlapping pathomechanisms, likely involving altered immune function in the brain.

**Keywords:** Alzheimer's disease, Dystrophic neurites, Microglia, PI3K-Akt signaling, Type 2 diabetes, Typical Western diet

## Background

Alzheimer's disease (AD) is the most common neurodegenerative disease. Typical AD pathology includes accumulation of neuritic plaques composed of  $\beta$ -amyloid peptide ( $A\beta$ ) aggregates, and dystrophic neurites positive for hyperphosphorylated Tau in the form of neurofibrillary tangles (NFTs) [1, 2]. Furthermore, activation of microglia, loss of synapses, and neuronal death are typically observed in AD [3]. Currently, available AD medication offers only a minor symptomatic relief, without any effects on the underlying pathogenic processes. Although AD has a strong genetic background, environmental and lifestyle factors, such as type 2 diabetes (T2D), play important roles in conferring the risk for AD [4]. T2D is characterized by insulin resistance in peripheral tissues, leading to increased serum insulin and glucose levels. Interestingly, AD and T2D share common features, such as impaired insulin signaling, increased levels of pro-inflammatory cytokines, metabolic changes, increased oxidative stress, and mitochondrial dysfunction [5]. However, the exact common underlying mechanisms between these two diseases remain elusive. Continuously increasing prevalence of both AD and T2D world-wide warrants for a better mechanistic understanding of the contribution of T2D on AD risk.

Lifestyle factors, such as lack of exercise and typical Western diet (TWD) containing high fat, high sugar, high cholesterol, and low fiber play a crucial role in the development of T2D. Likewise, epidemiological studies have revealed that the consumption of saturated fats, T2D, and obesity in midlife increase the risk of AD later in life [4, 6–10]. In mice, high-fat diet (HFD) and TWD lead to obesity, glucose intolerance and finally to full-blown T2D [11]. In most of the studies, HFD and TWD have led to impaired memory in both wild-type (WT) and AD transgenic mice [12–15]. Also, impaired insulin-Akt signaling in the brain of HFD/TWD animals has been often reported [16–18]. However, effects of HFD/TWD on  $\beta$ -amyloid and Tau pathology have been controversial [12, 13, 19–21].

In the brain, insulin plays a role as a neurotrophic factor and has also been linked to neuroinflammation, while neuronal glucose intake is mainly independent of the insulin-regulated GLUT-4 transporter [22, 23]. When insulin binds to insulin receptor (IR), it can activate two distinct branches of insulin signaling pathway: the Ras-mitogen-activated protein kinase (MAPK) and phosphoinositide 3-kinase (PI3K)-Akt-kinase pathways [24]. Akt-kinase controls the activity of glycogen synthase kinase 3 $\beta$  (GSK3 $\beta$ ). Reduced levels of GSK3 $\beta$  phosphorylation, specifically at the inhibitory S9 residue, in turn, result in augmented Tau phosphorylation [25]. Importantly, Akt-signaling also controls autophagic activity through mammalian target of Rapamycin complex 1 (mTORC1). Impaired autophagy is a common feature in AD and other neurodegenerative diseases [26]. Activation of PI3K-Akt-mTORC1 pathway by insulin or other stimuli inhibits autophagy, while nutrient starvation inactivates this pathway, and thus increases autophagic activity [27].

Inflammation is one of the key elements shared in both AD and T2D. Increased levels of proinflammatory cytokines, including tumor necrosis factor  $\alpha$  (TNF $\alpha$ ), are observed in adipose tissue of both obese and diabetic subjects as well as in the brain of AD patients [28, 29]. Recent genetic and functional studies have highlighted the relevance of the brain's innate immune cells in contributing to the onset and progression of AD [30, 31]. Specifically, studies have exemplified the emergence of reactive microglia subtypes in response to disease and damage, for which triggering receptor expressed on myeloid cells 2 (Trem2) has been identified as a central receptor [32, 33]. Transition of microglia from homeostatic to a disease-associated microglia (DAM) phenotype is a two-step process, in which Trem2-PI3K-Akt pathway plays a central role [32]. Furthermore, the deficits of Trem2 impair Akt-mTOR signaling in microglia, affecting autophagy and decreasing the ability of microglia to form a protective barrier around  $\beta$ -amyloid plaques, which eventually leads to increased formation of dystrophic neurites [34].

Here, we have studied the interaction between dietary (TWD) and genetic factors (APP<sup>swe</sup>/PS1<sup>dE9</sup> and Tau P301L mutations) and their effects on memory, brain pathology, and global gene expression in female mice with WT (AwTw) and different AD- and tauopathy-linked genetic backgrounds: Tau P301L (AwT+), APP<sup>swe</sup>/PS1<sup>dE9</sup> (A+Tw), and triple transgenic APP<sup>swe</sup>/PS1<sup>dE9</sup>/Tau P301L (A+T+). To our knowledge, this is the first time when all these mouse lines have been utilized in parallel in the same study to dissect the alterations in cellular pathways in the brain associated with TWD and different AD-associated pathologies. Our results suggest that TWD exacerbates age-related memory impairment in mice with a genetic predisposition to develop AD-like brain pathology as well as alters microglial gene expression and functionality. Supporting these findings, T2D also decreased the number of  $\beta$ -amyloid plaque-associated microglia also in frontal cortical biopsies of living idiopathic normal pressure hydrocephalus (iNPH) patients.

## Methods

### Animals

In this study, we used three transgenic mouse lines with C57Bl/6J background as models for AD and WT littermates with the same C57Bl/6J background as controls. The first mouse line coexpressed in a single transgene a chimeric mouse/human APP<sup>695</sup> harboring the Swedish K670M/N671L mutations (Mo/Hu APP<sup>swe</sup>) and human PS1 with the exon-9 deletion (PS1<sup>dE9</sup>) under mouse PrP promoter [35]. The second mouse line carried human Tau P301L mutation under CaMKII promoter [36]. The third line was created by crossing heterozygous line 1 and 2 mice resulting in APP<sup>swe</sup>/PS1<sup>dE9</sup> x Tau P301L mice. The study comprised of 46 female mice, 11 WT (AwTw), 13 APP<sup>swe</sup>/PS1<sup>dE9</sup> transgenic (A+Tw), 11 Tau P301L transgenic (AwT+) and 11 transgenic for both APP<sup>swe</sup>/PS1<sup>dE9</sup> and Tau P301L (A+T+). The dietary intervention started at the age of 7 months, so that half of the mice in each genotype group received a chow mimicking TWD (Adjusted Calories diet, TD 88137, Harlan Tecklad, Madison, WI, USA, with 21% w/w fat, 0.15% cholesterol and 35% sucrose) while the other half continued with standard rodent diet (STD) (5% w/w fat and 0% cholesterol) until sacrificed at the age of 13 months. The mice were weighed monthly. The mice were kept in a controlled environment (constant temperature, 22 ± 1 °C, humidity 50–60%, lights on 07:00–19:00), with food and water available ad libitum. All animal procedures were carried out in accordance with the guidelines of the European Community Council Directives 86/609/EEC and approved by the Animal Experiment Board of Finland.

### Glucose tolerance test (GTT)

GTT for mice was done at the age of 12 months. After 3 h of fasting in the morning, an i.p. injection of 1 mg/g D-glucose in a 20% solution (prepared in normal saline) was given. Blood samples for the determination of glucose levels (50–75  $\mu$ l) were collected at time points 0 (before glucose injection) and 30 min after the injection from the saphenous vein. The glucose values were determined immediately using a glucometer (One Touch, LifeScan Inc., Milpitas, CA, USA).

### Spontaneous activity

Spontaneous explorative activity was assessed by using an automated activity monitor (TruScan, Coulbourn Instruments, Whitehall, PA, USA) based on infrared photo-beam detection. The system consisted of an observation cage with white plastic walls (26 cm × 26 cm × 39 cm) and two frames of photo detectors enabling separate monitoring of horizontal (XY-move time) and vertical activity (rearing). The test cage was cleaned with 70% ethanol before each mouse to avoid odor traces. The following parameters were measured during a 10-min session: ambulatory distance (gross horizontal locomotion) and rearing time.

### Morris swim navigation test

Spatial learning and memory were assessed in the Morris swim task. The test was conducted in a white circular wading pool (diameter 120 cm) with a transparent submerged platform (diameter 14 × 14 cm) 1.0 cm below the surface serving for escape from the water. The pool was open to landmarks in the room (white screen blocking the view to the computer and the experimenter, green water hose, door, 1-m high black pattern on the wall). Temperature of the water was kept at 20 ± 0.5 °C. The acquisition phase was preceded by two practice days with a guiding alley to the platform (day -4 and day -3, not shown). During the acquisition phase (days 1–5), the location of the hidden platform was kept constant (SE quadrant) and the starting position varied between four different locations at the pool edge, with all mice starting from the same position in a given trial. Each mouse was placed in the water with its nose pointing towards the pool wall. If the mouse failed to find the escape platform within 60 s, it was placed on the platform for 10 s by the experimenter (the same time was allowed for mice that found the platform). The acquisition phase consisted of five daily trials with a 10 min inter-trial-interval. On day 5, the search bias was tested in a 60-s probe trial (the 5th trial) without the platform. The experimenter was blind to the genotype and treatment of the mice. The mouse was video-tracked, and the video analysis program calculated the

escape latency, swimming speed, path length and time in the pool periphery (10 cm from the wall) and in the platform zone (diameter 30 cm).

#### Passive avoidance test

This task was used as a control for long-term memory, since in contrast to Morris swim task, increased activity level leads to impaired performance in this task. The mouse was placed in the well-lit side of a two-compartment box and was freely allowed to enter the dark, closed compartment through a hole in the dividing wall. As soon as the mouse entered the dark side, the slide door separating the compartment was closed and a mild foot-shock delivered (2 × 2 s at 0.30 mA). The mouse was then taken to its home cage. The memory for the aversive experience was assessed 48 h later by taking the time for the mouse to enter the dark compartment with a cut-off time of 180 s.

#### Tissue sampling and preparation

At the end of the study, all mice were deeply anesthetized with intraperitoneal pentobarbiturate-chloralhydrate cocktail (60 mg/kg each) and transcardially perfused with ice-cold saline for 3 min to rinse blood from the brain. The brain was removed and placed on ice. For half of the mice, one brain hemisphere was immersion fixed in 4% paraformaldehyde, followed by 30% sucrose overnight and stored in antifreeze at -20 °C. The other hemisphere was dissected on ice into following blocks: frontal, parieto-occipital and temporo-occipital cortices, hippocampus, cerebellum and olfactory bulb. In addition, two lobes of liver, pancreas, gastrocnemius and tibialis anterior muscles and samples of inguinal and subcutaneous fat were dissected and snap frozen in liquid nitrogen. The samples were stored at -80 °C. The PFA 4% fixed hemispheres were cut using a freezing slide microtome into 35 µm coronal sections. The hippocampal tissue samples were collected into microcentrifuge tubes and weighed. Samples were homogenized in 250 µl of phosphate-buffered saline (DPBS, Lonza, Walkersville, MD, USA) using a stirrer. Fractions of homogenates were taken to RNA isolation (50 µl of homogenate and 500 µl Tri Reagent (Sigma-Aldrich, St. Louis, MO, USA) and Western blot analysis (100 µl of homogenate was supplemented with EDTA-free protease inhibitor cocktail (ThermoScientific, Waltham, MA, USA) and HALT™ phosphatase inhibitor cocktail (ThermoScientific, Waltham, MA, USA) 1:100. The remaining 100 µl of homogenate was left unprocessed and stored at -80 °C.

#### Histochemistry

Snap frozen liver blocks (originally designed for biochemistry) were cut with a cryostat into 5 µm sections

and stained with hematoxylin-eosin to reveal lipid vacuoles indicating a fatty liver change. Despite the freezing artefact, the vacuoles were clearly visible in most cases. Three sections of each mouse were analyzed by two researchers blinded to the genotype and treatment of the mice and scored as follows: 0 = no change, 1 = possible change, 2 = clear fatty-liver change. The brain hemispheres fixed in 4% paraformaldehyde were cut using a freezing slide microtome into 35 µm coronal sections. Three brain sections, 105 µm apart were selected between bregma -3.1 mm and -3.5 mm coronal planes according to the Paxinos and Franklin atlas [37]. IHC staining was done with fluorescent secondary antibodies for free-floating sections. First, the sections were pre-treated in 0.05 M citrate solution for 30 min (pH 6.0) at 80 °C. Endogenous peroxidase activity on sections was inhibited by incubation with 0.3% or 2% hydrogen peroxide in methanol. Non-specific antibody binding was blocked with 3% bovine serum albumin or 10% normal goat serum. To visualize β-amyloid burden and dystrophic neurites, the sections were stained with rabbit polyclonal anti-Pan-Aβ (1:2000, Aβ 1-40, Invitrogen, Carlsbad, CA, USA) and mouse monoclonal antihuman phospho-Tau (S202, T205) AT8 (1:1000, Thermo Fisher Scientific, MN1020, UK) for dystrophic neurites. Furthermore, dystrophic neurites were visualized using 22C11 antibody recognizing APP N-terminal epitope (1:2000, Millipore, MAB348) and β-amyloid plaques were co-stained using X-34 (SML1954, Sigma-Aldrich, St. Louis, MO, USA). Microglia were detected with rabbit polyclonal anti-Iba-1 (1:5000, #019-19,741, FUJIFILM Wako Chemicals Europe GmbH, Neuss, Germany). To see details of microglia around β-amyloid plaques, sections were stained with two sets of antibodies. β-amyloid plaques were stained with X-34 (SML1954, Sigma-Aldrich, St. Louis, MO, USA), microglia with rabbit polyclonal anti-Iba-1 (1:5000, #019-19,741, FUJIFILM Wako Chemicals Europe GmbH, Neuss, Germany) and lysosomes with rat monoclonal anti-Cd68 (clone FA-11, #MCA1957, Bio-Rad, Hercules, CA, USA). In the second set, p85 was stained with mouse monoclonal anti-p85 (1:1000, Antibodies-online GmbH, Aachen, Germany) along with Iba-1 staining. Primary antibodies were incubated overnight at +4 °C. For X-34 staining, the sections were incubated in X-34 solution for 1 h and briefly rinsed with 60% PBS / 40% EtOH solution prior to primary antibody incubation. The sections were incubated with appropriate fluorescent secondary antibodies: goat anti-mouse 488 (Invitrogen Alexa Fluor 488, A11029, Molecular Probes, Invitrogen, Eugene, OR, USA) for p85 and AT8, goat anti-rabbit 594 (Invitrogen Alexa Fluor 594, A11037, Molecular Probes, Invitrogen, Eugene, OR, USA) for Iba-1 and Pan-Aβ, and goat anti-rat 488 (Invitrogen Alexa Fluor 488, A1106, Molecular Probes,

Invitrogen, Eugene, OR, USA) for Cd68. The sections were mounted with Vectashield Hard Set with or without DAPI (Vector Laboratories, Burlingame, CA, USA) on gelatin-coated slides. Control sections without the primary antibodies were processed simultaneously, and no unspecific staining was observed.

#### Fluorescent microscopy and image analysis

The analysis of  $\beta$ -amyloid plaques and surrounding dystrophic neurites was done in the dentate gyrus (DG) and lateral entorhinal cortex (LEC) (Fig. 1i). Images were taken with a fluorescent microscope (Zeiss Axio Imager M2 microscope, Germany, with AxioCam ERc5s -camera attached). Both brain areas were imaged with 5x or 20x objectives. Brain areas were imaged with Z-stack imaging method, 12 layers with a total distance of 15  $\mu$ m. Counting of dystrophic neurites positive for AT8 antibody was done with direct microscopy. The analysis of 22C11-positive dystrophic neurites was performed using confocal microscopy (below). The ZEN 2012 software Blue edition (Carl Zeiss Microimaging GmbH) was used for image processing. The  $\beta$ -amyloid plaque burden was determined with Adobe Photoshop CS6 extended (version 13.0  $\times$  32). To estimate the total  $\beta$ -amyloid burden in the studied brain regions, we measured the total area of  $\beta$ -amyloid plaques with the most representative threshold, same for all animals, within the defined ROI (LEC and HC) in three brain sections and divided the area by the ROI area. Thus, the  $\beta$ -amyloid burden was expressed as an average percentage from three brain sections. All plaques over 9.9  $\mu$ m diameter in both brain areas, LEC and HC, were counted as well as dystrophic neurites around each plaque. Counting was done by an investigator blinded to the genetic and dietary background of mice.

#### Confocal microscopy and image analysis

Details of microglia around  $\beta$ -amyloid plaques were analyzed from fluorescent images of the molecular layer of dentate gyrus obtained with a Zeiss Axio Observer inverted microscope equipped with a Zeiss LSM 700 or Zeiss LSM 800 confocal module (Carl Zeiss Microimaging GmbH, Jena, Germany) using 63  $\times$  (NA 1.4) oil objective for CD68 and p85 stainings, and 20  $\times$  (NA 0.5) objective for 22C11 staining. For 22C11 analysis, six z-stack images (15.17  $\mu$ m with 2.17  $\mu$ m optical sections) were collected per brain section. For Cd68 and p85 analyses, at least three z-stack images (9  $\mu$ m with 0.9  $\mu$ m optical sections) were collected per brain section. Laser and detector settings were maintained constant for each immunostaining. All image processing and analyses were performed with Fiji software [38]. Area and intensity of the immunofluorescence signals were analyzed using automated scripts. Maximum intensity projections were

generated for each channel and rolling ball algorithm and Gaussian blurring were applied to subtract background and remove noise, respectively. The immunostainings were segmented using Otsu automatic threshold for X-34, Intermodes automatic threshold for 22C11, and Moments automatic threshold for Iba1, Cd68, and p85. For the analysis of Cd68 and Iba1, the outlines of a  $\beta$ -amyloid plaque were first determined from the X-34 staining, then 22C11, Cd68, and Iba1 immunoreactive area and intensity were analyzed within 30  $\mu$ m from the plaque outline. When analyzing p85, outlines of  $\beta$ -amyloid plaque was assessed manually due to a lack of X-34 staining, and then p85 staining area and intensity were analyzed within 30  $\mu$ m from the plaque outline. For the analysis of microglial morphology, Iba1 staining around  $\beta$ -amyloid plaques was segmented using Gaussian blurring and automatic Li threshold algorithm, and the resulting binary image was skeletonized. The skeletonized images were visually evaluated, and only skeletons representing an individual microglial cell were selected for further analysis using AnalyzeSkeleton (2D/3D) plugin. Imaging and analysis of the immunostainings was done by investigators blinded to the genetic or dietary background of mice.

#### iNPH cohort for cortical brain biopsies

Patients characterized in Table 1, were diagnosed with probable iNPH [39] and selected for CSF shunt surgery according to the previously described protocol [40] in Department of Neurosurgery Kuopio University Hospital from 2012 until 2017. Diagnostic right frontal cortical brain biopsy was taken during shunt surgery and occurrence of  $\beta$ -amyloid and/or phospho-Tau was evaluated by neuropathologist as described previously [41]. According to the neuropathological examination, all the individuals included in this study were  $\beta$ -amyloid positive but phospho-Tau (AT8) negative. Homeostatic Model Assessment of Insulin Resistance (HOMA-IR) was assessed using the formula from: <https://www.thebloodcode.com/homa-ir-calculator/>. All patients gave their written informed consent, prior to the surgery, for the study accepted by Ethics Committee, Hospital District of Northern Savo.

#### Immunohistochemistry of human biopsy brain tissue

The biopsy samples were fixed in buffered formalin overnight and subsequently embedded in paraffin. Five micrometers deparaffinized sections were used for IHC staining. Antigen retrieval was performed by boiling the sections in 10 mM Tris – 1 mM EDTA buffer, pH 9.0, in pressure cooker for 10 min, followed by cooling to room temperature and incubation in 80% formic acid for 20 min. Endogenous peroxidase activity was quenched by incubation in 1% H<sub>2</sub>O<sub>2</sub> and unspecific antibody binding

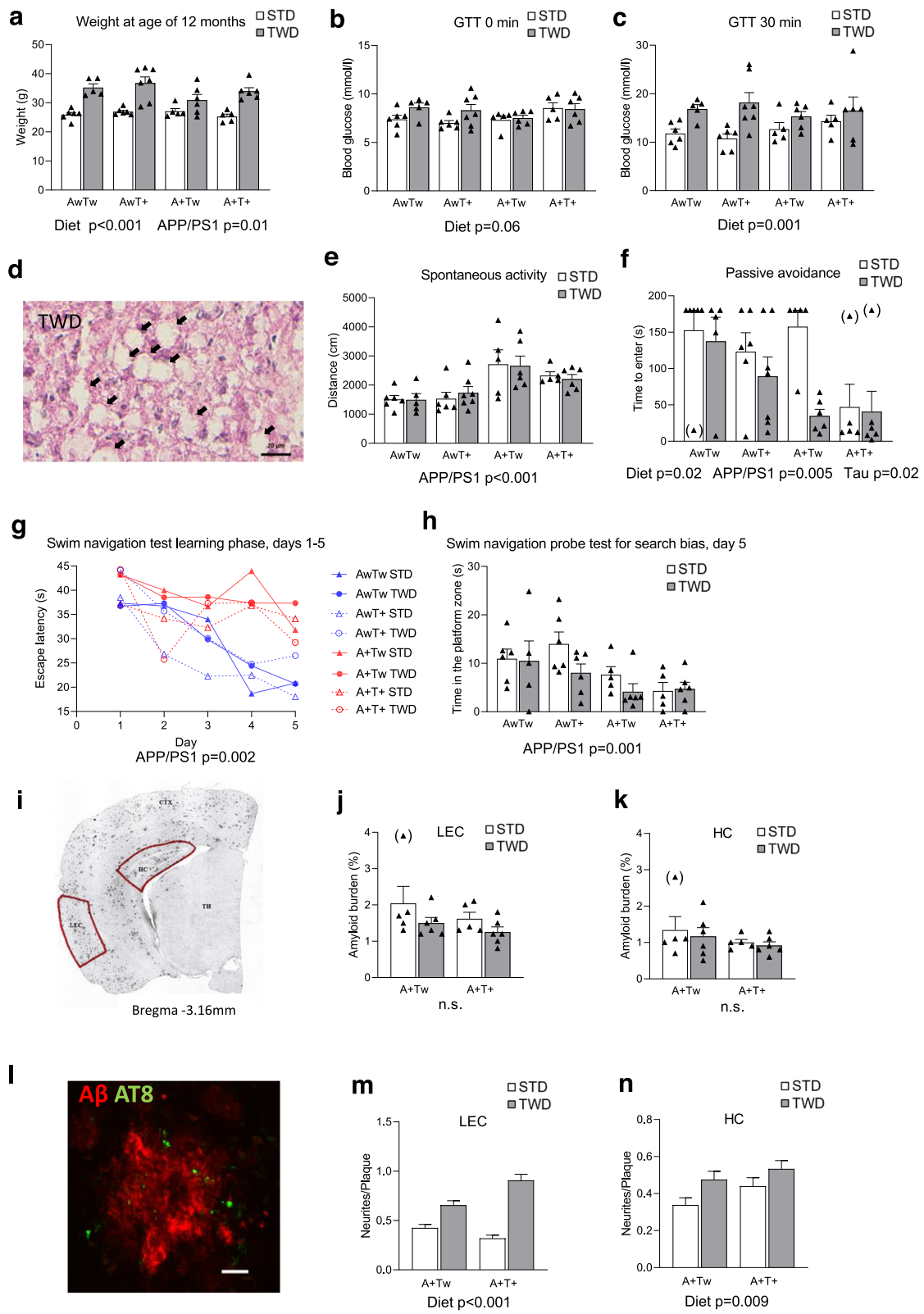


**Fig. 1** (See legend on next page.)

(See figure on previous page.)

**Fig. 1** TWD leads to T2D, memory impairment and increased number of dystrophic neurites in mice with AD-linked genetic backgrounds. **a** Weight of mice at age of 12 months (Two-way ANOVA). **b** Glucose tolerance test (GTT) results after 3 h fasting (Two-way ANOVA). **c** Serum glucose levels in GTT after 30 min of D-glucose injection ( $p = 0.001$ , Two-way ANOVA). **d** Representative liver sample image of TWD. Mice with TWD had significantly higher fatty liver score as compared to mice with STD ( $p < 0.001$ , Mann-Whitney). Black arrows indicate lipid vacuoles. Scale bar 20  $\mu\text{m}$ . **e** Assessment of spontaneous activity ( $p < 0.001$ , Two-way ANOVA). **f** Passive avoidance test revealed impaired performance of mice with TWD as compared to mice with STD (diet effect,  $p = 0.02$ , Two-way ANOVA). Also, AD and tauopathy-associated transgenes impaired the performance (A+ = APPswe/PS1dE9;  $p < 0.001$  and T+ = Tau P301L;  $p < 0.001$ , Two-way ANOVA). Three outliers were left out from statistical analysis (in brackets). **g** In five-day learning phase of Morris swim navigation test, mice with A+ transgene (APPswe/PS1dE9) (red lines) did not learn to find the platform as fast as mice without A+ transgene (blue lines,  $p = 0.002$ , Two-way ANOVA), while TWD and T+ transgene (Tau P301L) did not affect learning. **h** On day five, mice with A+ transgene spent significantly less time in platform zone ( $p = 0.001$ , Two-way ANOVA). Also, mice with TWD spent less time in platform zone as compared to mice with STD, but the difference did not reach statistical significance ( $p < 0.09$ , Two-way ANOVA). **i** A representative image of APPswe/PS1dE9 mouse coronal brain section used for assessing  $\beta$ -amyloid plaque load from lateral entorhinal cortex (LEC) and from dentate gyrus (DG) of hippocampus (HC). **j** Amyloid burden quantification in LEC, and **k** in HC. **l** A representative fluorescence microscope image of APPswe/PS1dE9 mouse coronal brain section showing AT8-positive dystrophic neurites around  $\beta$ -amyloid plaques. Scale bar = 10  $\mu\text{m}$ . **m** Quantification of dystrophic neurites/plaque in LEC showing significant increase in TWD mice as compared to STD mice ( $p < 0.001$ ). **n** Also, in HC number of dystrophic neurites per plaque was increased in TWD mice as compared to STD mice ( $p = 0.009$ ). All results are shown as mean + SEM, behavioral tests:  $n = 5-7$  mice/group, Two-way ANOVA, immunohistochemistry:  $n = 5-6$  mice/group, 3 brain slices/mouse. Dystrophic neurites around  $\beta$ -amyloid plaques (diameter > 10  $\mu\text{m}$ ) were counted, Kruskal-Wallis H-test. AwTw = wild-type, AwT+ = Tau P301L, A + Tw = APPswe/PS1dE9, A + T+ = APPswe/PS1dE9 x Tau P301L

was blocked using 3% bovine serum albumin (BSA). Sections were incubated with the first primary antibody, rabbit polyclonal anti-Iba-1 (#019-19,741, 1:1500, FUJIFILM Wako Chemicals Europe GmbH, Neuss, Germany) overnight at 4 °C, followed by visualization with biotinylated anti-rabbit secondary antibody (1:200, Vector Laboratories, Burlingame, CA, USA) and Vectastain Elite ABC Kit Peroxidase (Vector Laboratories, Burlingame, CA, USA) using 3,3'-diaminobenzidine (DAB, Sigma-Aldrich, St. Louis, MO, USA) as chromogen with 1 min 30s incubation time. Staining of the second

antigen started with blocking with 3% BSA and incubation with the second primary antibody, mouse monoclonal anti-A $\beta$  (anti- $\beta$ -amyloid 17-24, clone 4G8, #800712, 1:500, Biologend, San Diego, CA, USA) overnight at 4 °C. Staining was visualized with biotinylated anti-mouse secondary antibody (1:200, Vector Laboratories, Burlingame, CA, USA) and Vectastain ABC-AP Kit (Vector Laboratories, Burlingame, CA, USA), and 30-min incubation with Permanent AP Red Kit substrate/chromogen (Zytomed Systems GmbH, Berlin, Germany). Sections were counterstained with Mayer's haematoxylin and

**Table 1** Demographics, clinical status, and pathology of iNPH cases

Group	Gender	Age (years)	Weight (kg)	Height (cm)	BMI <sup>a</sup>	HOMA-IR <sup>b</sup>	T2D <sup>c</sup>	Hypertension	A $\beta$ pathology	APOE genotype
<b>BMI &lt; 25</b>	Female	67	70	170	24.2	0.6	no	no	positive	34
	Male	79	65	168	23	2.7	no	no	positive	34
	Male	75	56	159	22.2	0.7	no	yes	positive	44
	Female	71	60	158	24	1.9	no	no	positive	33
	avg.	73	63	164	23.4	1.5				
<b>BMI &gt; 30</b>	Female	71	87	160	34	4.9	no	no	positive	34
	Male	81	102	171	34.9	7	no	no	positive	33
	Male	69	80	160	31.3	3.4	no	yes	positive	33
	avg.	73.5	89.8	166	32.6	5.1				
<b>BMI &gt; 30 + T2D</b>	Male	72	98	170	33.9	14.1	yes	yes	positive	33
	Male	73	90	173	30.1	4.7	yes	yes	positive	34
	Male	73	92	162	35.1	4.5	yes	yes	positive	33
	Female	75	92	155	38.3	16.8	yes	yes	positive	34
	Male	67	82	165	30.1	5.9	yes	yes	positive	34
	avg.	72	90.8	165	33.5	9.2				

Age, Weight, Height, BMI and clinical status when biopsy was taken

<sup>a</sup> Body Mass Index, weight (kg) / [height (m)]<sup>2</sup>

<sup>b</sup> Homeostatic Model Assessment for Insulin Resistance

<sup>c</sup> Type 2 Diabetes

mounted with aqueous mounting medium (Aquatex, Merck, Darmstadt, Germany). Control sections without the primary antibodies were processed simultaneously, and no unspecific staining was observed.

#### Imaging and analysis of human brain biopsy tissue

The human biopsy brain tissue sections were imaged with Hamamatsu NanoZoomer-XR Digital slide scanner with 20x (NA 0.75) objective (Hamamatsu Photonics K.K.). Due to the small size of the biopsy specimen, all plaques with microglia within or around the plaque in the grey matter area of the specimen were included in the analysis. Size of the  $\beta$ -amyloid plaques was obtained by manually outlining the plaques in NDP.view2 software (Hamamatsu Photonics K.K.). Plaque-associated microglia were manually counted, and the number of microglia within the plaque area and around the plaque area were recorded separately. Only microglia with clearly visible soma were included in the count. Counting and analysis was performed by an investigator blinded to sample identity.

#### Cell cultures and treatments

Immortalized mouse microglial BV2 cells were grown in RPMI-1640 medium (Sigma-Aldrich, St. Louis, MO, USA) supplemented with 10% fetal bovine serum (FBS, Gibco, Waltham, MA, USA), 2 mM L-glutamine (Lonza, Basel, Switzerland) and 1% penicillin-streptomycin (P/S: 100 U/ml penicillin and 100 U/ml streptomycin, Lonza, Basel, Switzerland) in 15 cm cell culture plates (Nunc, Roskilde, Denmark) as previously described [42]. To study the effects of PI3K inhibition on Syk phosphorylation, BV2 cells were scraped from confluent plate on RPMI-1640 medium without FBS to induce serum starvation. Cells were diluted to concentration  $1 \times 10^6$  cells/ml, and cell suspension was divided into 1.5 ml Eppendorf tubes. After 1 h, PI3K inhibitor treatment with 1  $\mu$ M LY294002 (Life Technologies, Frederick, MD, USA) was started. After 1 h 40 min, Src-kinase inhibitor (2  $\mu$ M SU 6656, S9692 Sigma-Aldrich, St. Louis, MO, USA) was added. At 2 h time point, cells were treated with M-CSF (100 ng/ml) Recombinant Human M-CSF (Macrophage-Colony Stimulating Factor, BioLegend cat. 574,806, San Diego, CA, USA) for 5 min. Tubes were placed on ice and subsequently centrifuged at 10000 x g for 1 min at +4 °C. Supernatant was removed and cells were lysed with tissue protein extraction buffer (T-PER, ThermoScientific, Rockford, IL, USA) including EDTA-free protease inhibitor cocktail (ThermoScientific, Waltham, MA, USA) and HALT™ phosphatase inhibitor cocktail (ThermoScientific, Waltham, MA, USA) 1:100, and incubating on ice for 30 min. The lysates were centrifuged at 16000 x g for 10 min at +4 °C, the protein lysates were collected into the new tubes and stored at –

20 °C. Effects of PI3K inhibition on Syk phosphorylation in mouse WT primary microglia was studied by plating 100,000 cells in 96-well plate in Dulbecco's modified Eagle's medium (DMEM, Lonza, Verviers, Belgium) supplemented with 2 mM L-glutamine (Lonza, Verviers, Belgium) and 1% P/S (Lonza, Verviers, Belgium), but without FBS in order to induce serum starvation. After 1 h, PI3K inhibitor treatment with 1  $\mu$ M LY294002 (Life Technologies, Frederick, MD, USA) was started. After 2 h, cells were treated with Trem2 antibody (R&D Systems, Minneapolis, MN, USA) with final concentration of 10  $\mu$ g/ml. After 5 min antibody treatment, plate was placed on ice, cells were lysed and supernatants were analyzed with phosphoSyk Alpha-LISA kit (PerkinElmer, Waltham, MA, USA) according to the kit instructions. Mouse primary microglia cultures from Akt2 knock-out (KO) (Mouse B6.129P2(Cg)-Akt2tm1.1Mbb/J, The Jackson Laboratory, Bar Harbor, Maine, USA) and C57BL/6 WT mice were prepared as previously [43]. Briefly, brains of neonatal (P0–P2) mice were dissected and meninges were removed. Brain tissue was dissociated using mechanical shearing and trypsin. Cells of two brains were plated on poly-L-lysine (Sigma-Aldrich, St. Louis, MO, USA) coated T75 culture flasks and cultured in Dulbecco's modified Eagle's medium (DMEM, Lonza, Verviers, Belgium) supplemented with 10% FBS (Gibco, Waltham, MA, USA), 2 mM L-glutamine (Lonza, Verviers, Belgium) and 1% P/S (Lonza, Verviers, Belgium). On the next day, the cells were washed three times with PBS (DPBS, Lonza, Walkersville, MD, USA) to remove cellular debris and cultured with fresh DMEM with supplements. After 7 days, mature microglia were shaken off from the astrocytic feeding layer. Microglial cells were counted, and appropriate number of cells was plated in 96 well plates and used for assessing phagocytic activity and responses to inflammatory activation.

#### Phagocytosis assay

For pHrodo phagocytosis assays, BV2 cells were plated on 96-well plates (Nunc, Roskilde, Denmark) at 4000 cells/well 16 h before starting the assay. Primary microglia were cultured in 96-well plates at 20,000 cells/well in volume of 100  $\mu$ l in DMEM culture medium with supplements described above. Cells were treated with PI3K inhibitor LY294002 (Life Technologies, Frederick, MD, USA) with different concentrations and with 5  $\mu$ M Cytochalasin D (Sigma-Aldrich/Merck, St. Louis, MO, USA), inhibitor of actin polymerization, which served as negative control by blocking the phagocytosis. After 1 h pretreatment with the inhibitors, cells were treated with pHrodo Zymosan bioparticles (Essen BioScience, Ann Arbor, MI, USA) with a final amount of 5  $\mu$ g/well. Three to four wells were used for each treatment condition. Time-lapse videomicroscopy sequences of living



cells were obtained using the IncuCyte S3 system (Essen BioScience, Ann Arbor, MI, USA) with 20x (BV2) or 10x (primary microglia) objective lenses, and images from 4 fields per culture well were obtained every 15 min (BV2) or every 30 min (primary microglia) for up to 3 h. pHrodo red fluorescent signal was used as an indicator of uptake by the lysosomal cell compartments. After 3 h, nuclei of cells were stained with 1  $\mu$ M Vybrant DyeCycle Green (Molecular probes/ThermoFisher Scientific, Eugene, OR, USA) and imaged with IncuCyte in order to count the cells. Area ( $\mu\text{m}^2$ ) of red fluorescence per image was calculated for each time point, normalized to total cell count, and plotted as a time course.

### Western blot analysis

The inhibitor-supplemented total protein fractions were further diluted by taking 50  $\mu$ l of homogenate and adding 70  $\mu$ l of T-PER Tissue Protein Extraction Reagent (ThermoScientific, Rockford, IL, USA). After incubating for 20 min on ice, samples were centrifuged for 10 min at 16,000  $\times$  g and the supernatant was transferred into a new microcentrifuge tube. Protein concentrations were measured using the Pierce BCA Protein Assay Kit (ThermoScientific, Waltham, MA, USA). Total protein lysates (15–50  $\mu$ g) were subjected to SDS-PAGE using NuPAGE 4–12% Bis-Tris Midi Protein Gels (Invitrogen, Carlsbad, MA, USA) and subsequently transferred to Polyvinylidene difluoride (PVDF) membranes using the iBlot 2 Dry Blotting System (Invitrogen, Carlsbad, MA, USA). Unspecific antibody binding was prevented by incubating the blots in blocking solution containing 5% non-fat milk or 5% BSA (Sigma-Aldrich, St. Louis, MO, USA) in 1x Tris-buffered saline with 0.1% Tween 20 (TBST) for 1 h at RT. Proteins were detected from the blots using the following primary antibodies diluted in the appropriate ratio with 1x TBST and incubated overnight at + 4 °C: rabbit anti-phospho-Akt1 (S473, 1:1000, #9018, Cell Signaling Technology, Danvers, MA, USA), rabbit anti-phospho-Akt2 (S474, 1:1000, #8599, Cell Signaling Technology, Danvers, MA, USA), rabbit anti-phospho-Akt (Thr308/309/305, 1:1000, #13038, Cell Signaling Technology, Danvers, MA, USA), rabbit anti-Akt1 (1:1000, #75692, Cell Signaling Technology, Danvers, MA, USA), rabbit anti-Akt2 (1:1000, #3063, Cell Signaling Technology, Danvers, MA, USA), rabbit anti-Akt (1:1000, #9272, Cell Signaling Technology, Danvers, MA, USA), rabbit anti-phospho-GSK3 $\beta$  (S9, 1:1000, #9336, Cell Signaling Technology, Danvers, MA, USA), rabbit anti-GSK3 $\beta$  (1:1000, #9315, Cell Signaling Technology, Danvers, MA, USA), custom-made mouse anti-phospho-Tau (B6, 1:1000) [44], mouse anti-4R-Tau (RD4, 1:1000, 05–804, Millipore), mouse anti-SQSTM1/p62 (1:1000, #5114, Cell Signaling Technology, Danvers, MA, USA), mouse anti-LC3 (1:1000, ab51520, Abcam, Cambridge,

UK), mouse anti-Caspase-3 (1:1000, #9662, Cell Signaling Technology, Danvers, MA, USA), mouse anti-phospho-ERK (1:500, sc-7383, Santa Cruz Biotechnology, Dallas, TX, USA), rabbit anti-ERK2 (1:500, sc-154, Santa Cruz Biotechnology, Dallas, TX, USA), mouse anti-p85 $\alpha$  (1:1000, ABIN1098111, Antibodies-online GmbH, Aachen, Germany), rabbit anti-phospho-SYK (1:1000, MA5–14918, Invitrogen, Waltham, MA, USA), rabbit anti-SYK (1:1000, #13198, Cell Signaling Technology, Danvers, MA, USA), mouse anti- $\beta$ -actin (1:1000, ab8226, Abcam, Cambridge, UK) and mouse anti-GAPDH (1:15000, ab8245, Abcam). Blots were subsequently probed with the appropriate horseradish peroxidase (HRP)-conjugated secondary antibodies, either sheep anti-mouse-HRP (1:5000, NA931V, GE Healthcare, Chicago, IL, USA) or donkey anti-rabbit-HRP (1:5000, NA934V, GE Healthcare, Chicago, IL, USA) diluted in 1x TBST and incubated for 1 h at room temperature. Enhanced chemiluminescence (ECL, GE Healthcare, Chicago, IL, USA) was used to detect the protein bands. Blots were imaged with the Chemidoc MP system (Bio-Rad, Hercules, CA, USA) and images were quantified using the ImageLab (Bio-Rad, Hercules, CA, USA) software.

### AlphaLISA assay

Phospho-Syk level from WT mouse primary microglia cultures were determined using AlphaLISA SureFire Ultra kit (PerkinElmer, Waltham, MA, USA) according to manufacturer's instructions. Briefly, after treatments, cells were lysed in freshly prepared 1X Lysis buffer (40  $\mu$ l/well) and agitate on a plate shaker (~ 350 rpm) for 10 min at room temperature. Thirty microliters of the lysate was transferred to a 96-well 1/2Area-Plate™ for assay. Acceptor Mix was added (15  $\mu$ l/well) and plate was sealed with Topseal-A adhesive film. Plate was incubated for 1 h at room temperature covered with foil. Donor Mix was added to wells (15  $\mu$ l/well) under subdued light. Plate was sealed with Topseal-A adhesive film, covered with foil, and incubated for 1 h at room temperature in the dark. Plate was analyzed with EnVision plate reader (PerkinElmer, Waltham, MA, USA), using standard AlphaLISA settings.

### ELISA and nitric oxide assays

A $\beta$ 40 and A $\beta$ 42 levels in the mouse hippocampus homogenates were determined with monoclonal and HRP-conjugated antibody-based Human/Rat  $\beta$  amyloid 40 ELISA kit (Wako, Osaka, Japan). Mouse TNF- $\alpha$  and IL-6 ELISA Ready-SET-Go! kits (Affymetrix, San Diego, CA, USA) were used for the detection of tumor necrosis factor  $\alpha$  (TNF- $\alpha$ ) and IL-6 in the conditioned media of WT and Akt2 KO mouse primary microglia cultures treated

with LPS (200 ng/ml, Sigma-Aldrich, St. Louis, MO, USA) and IFN $\gamma$  (20 ng/ml, Sigma-Aldrich, St. Louis, MO, USA) for 24 h. Nitric oxide (NO) levels were determined using the Griess Reagent Kit for Nitrite Determination (G-7921, Life Technologies, Eugene, OR, USA). All kits were used as recommended by the manufacturers.

### Real time quantitative PCR analysis

RNA was isolated from mouse hippocampus homogenates using the Direct-zol RNA MiniPrep (Zymo Research, Irvine, CA, USA). RNA concentrations were measured using the NanoDrop ND-1000 spectrophotometer (Thermo Fisher Scientific, Waltham, MA, USA). Total of 250 ng of RNA was subsequently synthesized into cDNA using the Transcriptor First Strand cDNA Synthesis Kit (Roche Diagnostics, Risch-Rotkreuz, Switzerland). RT-qPCR was subsequently run using the LightCycler 480 Instrument II (Roche Diagnostics, Risch-Rotkreuz, Switzerland) with the LightCycler 480 SYBR Green I Master (Roche Diagnostics, Risch-Rotkreuz, Switzerland) and the following primers (TAG Copenhagen, Copenhagen, Denmark): mouse *Pik3r1* forward 5'-TATTGCGAGGGAAGCGAGAC-3', mouse *Pik3r1* reverse 5'-ACTTCGCCGTCTACCACTAC-3', mouse *Trem2* forward 5'-TGG AAC CGT CAC CAT CAC TC-3', mouse *Trem2* reverse 5'-TGG TCA TCT AGA GGG TCC TCC-3', mouse *Tyrbp* forward 5'-ACC CGG AAA CAA CAC ATT GC-3', mouse *Tyrbp* reverse 5'-TTG CCT CTG TGT GTT GAG GT-3', mouse  $\beta$ -actin forward F: 5'-GGCTGTATTCCCCTCC ATCG-3', mouse  $\beta$ -actin reverse R: 5'-CCAGTTGGTA ACAATGCCATGT-3'. Results were calculated using the 2- $\Delta\Delta$ Ct method [45].

### RNA sequencing

Library preparation and sequencing was conducted in Finnish Functional Genomics Centre (FFGC), Turku Centre for Biotechnology, University of Turku and Åbo Akademi University. The quality of the total RNA samples as well as prepared libraries was ensured with Advanced Analytical Fragment Analyzer. Sample and library concentration were measured with Qubit<sup>®</sup> Fluorometric Quantitation, Life Technologies. Library preparation was done according to Illumina TruSeq<sup>®</sup> Stranded mRNA Sample Preparation Guide (part # 15031047). The 45 libraries with good quality were pooled in one pool and run in 2 lanes. The samples were sequenced using Illumina HiSeq 3000 instrument to a minimum read depth of 12 million reads per sample. Single-read sequencing with 1 × 50 bp read length was used, followed by 8 + 8 bp dual index run.

### Quality control and transcript abundance quantification

FastQC version 0.11.8 (<http://www.bioinformatics.babraham.ac.uk/projects/fastqc/>) was used to examine the quality of the RNA sequencing reads. Illumina sequencing adapter sequences were removed, and reads were quality trimmed using the Trimmomatic version 0.38 [46]. The obtained trimmed reads were then mapped against the ribosomal and mitochondrial reference sequences (build mm10) using the Bowtie 2 version 2.2.3 [47]. Successfully mapped reads were abandoned. The rest of the reads were subjected to pseudo alignment to mouse reference transcriptome (build mm10) and transcript abundance quantification using kallisto version 0.44.0 [48]. Additionally, reads were aligned to human reference transcriptome (hg38) to quantify human *APP*, *PSENI* and *MAPT* expression levels (Supplementary Fig. 2a).

### Differential expression analysis

Transcript abundance estimates were collapsed to gene-level counts using R package tximport version 1.10.1 [49]. Gene-level counts were pre-filtered (mean of gene count > 10), normalized and variance stabilizing transformed using R package DESeq2 version 1.22.2 [50]. Potentially confounding batch effects were corrected using removeBatchEffect function from limma version 3.38.3 [51]. The differentially expressed genes between diet and genotype groups were analyzed using the DESeq2.

### Consensus weighted gene co-expression network analysis

We carried out Consensus Weighted Gene Co-expression Network Analysis (WGCNA) as described previously [52]. Since the experimental design contains two variables of interest (genotype and diet), we carried out a consensus network analysis of two datasets: data from AwTw, AwT+, A+Tw, and A+T+ mice on STD, and data from the same genotypes with TWD. The rationale is that a consensus analysis identifies modules that group together genes correlated in both datasets, i.e., both with respect to diet as well as genotype. A thresholding power of 6 was chosen as it was the smallest threshold that resulted in a scale-free R<sup>2</sup> fit of 0.8). The “signed hybrid” network was used (deepSplit = 4, minModuleSize = 40) in which negatively correlated genes are considered unconnected. This analysis identified 28 co-expression modules ranging from 52 to 2728 genes per module (Supplementary Table 1). Genes in each module were further represented by a single representative expression profile (module eigengene, 1st principal component of the module). Module eigengenes were correlated with genotype to determine the association of co-expressed genes with genotype. Additionally, module eigengenes allow one to define a continuous measure of membership of all genes in all modules.

Genes with high module membership in a module are called hub genes for the module. To perform differential analysis of the consensus module networks (STD and TWD ~ genotype networks) we correlated and hierarchically sorted the identified module eigengenes for each network. Evaluation of module connectivity conservation was done by comparison of module sorting in their respective dendrograms.

#### Gene set enrichment analysis

We used the R package *anR* (<https://horvath.genetics.ucla.edu/html/CoexpressionNetwork/GeneAnnotation/>) to calculate the enrichment of co-expression gene modules in a collection of reference gene sets that includes Gene Ontology terms, KEGG pathways, literature gene sets collected in the *userListEnrichment* R function [53], Molecular Signatures Database gene sets [54], aging gene sets from *Enrichr* [55], microglia-relevant gene sets from several recent articles [32, 33, 56–59] and other gene sets. Fisher's exact test was used to evaluate overlap significance.

#### Transcription factor enrichment analysis

Over-represented transcription factor binding motifs (TFBS) and potential transcription factors (TF) in the surroundings of the transcription start site (TSS) of the differentially expressed genes (adjusted  $p$ -value < 0.005 due to diet) were identified using R package *RcisTarget* version 1.4.0 [60]. We used genome wide TFBS ranking database containing regions from 500bp\_upstream\_and\_100bp\_downstream from TSS (motif collection *mc9nr/mm10*). Identified significantly enriched TFBS (normalized enrichment score (NES) threshold > 4.0) were annotated to TFs by using provided annotation database.

#### Cell type enrichment analysis

Cell type enrichment was determined by cross-referencing of module genes with lists of genes known to be preferentially expressed in different cell types in mouse brain [61, 62]. All identified genes were used as background. Significance of enrichment of cell type markers with clusters was assessed using one tailed Fisher's exact test.

#### Statistics

IBM SPSS version 25 and R were used to analyze the data. Kolmogorov-Smirnov test was used first to test the normality of the distributions. The body weight at 12 months of age, blood glucose levels in the glucose tolerance test, spontaneous activity, latency to enter on day 2 in passive avoidance and search bias in the Morris swim task were analyzed with two-way ANOVA with A genotype (Aw vs A+), T genotype (Tw vs T+), and diet (STD vs TWD) as between-subject factors. The task

acquisition across days in Morris swim task was assessed with a mixed ANOVA for repeated measures (ANOVA-RM) using day as the within-subject and A and T genotypes as between-subject factors.  $\beta$ -Amyloid plaque load and the number of dystrophic neurites around plaques were analyzed separately for LEC and HC among A+ transgenic mice with two-way ANOVA using the T genotype and diet as factors. Statistical comparisons of biochemical analysis results were performed using two-way ANOVA followed by Fisher's Least Significant Difference (LSD) post-hoc test. Statistical comparisons of correlations were performed using Spearman's rho test. Results are expressed as mean  $\pm$  standard error of mean (SEM) of control samples.  $P$ -values < 0.05 were considered statistically significant.

## Results

### Feeding of mice with TWD results in T2D

At the beginning of the dietary intervention, mice in the different test groups weighed on average between 22.5–24.4 g. There was no difference between APP<sup>swe</sup>/PS1<sup>dE9</sup> genotypes (Aw vs. A+,  $p = 0.32$ ), or Tau P301L genotypes (Tw vs. T+,  $p = 0.57$ ) but mice in the to-be STD groups tended to weigh more than mice in the to-be TWD groups,  $p = 0.04$ . During the 6-month dietary intervention, there was a significant diet effect on the body weight increase ( $F_{6,33} = 25.6$ ,  $p < 0.001$ ), while the weight gain was less robust in mice with the A+ transgene (APP<sup>swe</sup>/PS1<sup>dE9</sup>) on TWD as compared to Aw mice ( $p = 0.01$ ) (Fig. 1a). In the GTT, baseline glucose levels were higher ( $F_{1,38} = 3.8$ ,  $p = 0.06$ ; Fig. 1b) and 30 min glucose levels robustly elevated ( $F_{1,38} = 13.9$ ,  $p = 0.001$ ; Fig. 1c) in TWD groups as compared to STD groups. A possible fatty liver change was assessed in hematoxylin-eosin stained liver sections and blindly scored by two raters. Evidence of lipid vacuoles was found in 20/24 mice (69%) fed with TWD, but only in 5/22 mice (23%) fed with STD. Additionally, clear fatty liver changes were found in 12/24 TWD mice (50%), and in none of the STD mice (Fig. 1d). The diet effect was highly significant on the fatty liver score ( $p < 0.001$ , Mann-Whitney), while neither A ( $p = 0.32$ ) nor T ( $p = 0.19$ ) genotype influenced the score. In summary, feeding the mice with TWD results in a phenotype related to T2D irrespective of genotype.

### TWD exacerbates memory impairment associated with $\beta$ -amyloid pathology

Previous studies have demonstrated that transgenic mice overexpressing the APP<sup>swe</sup>/PS1<sup>dE9</sup> mutation are hyperactive [63, 64]. Here, A+ mice traversed a significantly longer distance during the 10-min test time than Aw mice ( $F_{1,38} = 15.7$ ,  $p < 0.001$ ), whereas the T genotype ( $p = 0.43$ ) or diet ( $p = 0.84$ ) did not influence

spontaneous locomotion (Fig. 1e). Thus, to rule out the possible confounding effect of hyperactivity associated with the A+ genotype, we chose spatial navigation, where hyperactivity may speed up learning, and passive avoidance, where hyperactivity is unfavorable for the outcome, as tests for assessing possible memory impairment. In passive avoidance, all three factors (diet, A+, and T+ genotypes) showed a significant effect on the latency to enter the punished dark compartment, 48 h after the learning episode. A+ mice performed worse as compared to Aw mice ( $F_{1,38} = 8.8$ ,  $p = 0.005$ ), T+ mice worse than Tw mice ( $p = 0.02$ ) and TWD mice worse as compared to STD mice ( $p = 0.02$ ) (Fig. 1f). In the acquisition phase of Morris swim navigation task, there was no difference between the groups in their swimming speed (for all main effects  $p > 0.60$ ). A+ mice had significantly longer escape latencies than Aw mice ( $F_{1,38} = 11.6$ ,  $p = 0.002$ ), whereas the T genotype ( $p = 0.27$ ) and diet ( $p = 0.46$ ) did not influence escape latencies (Fig. 1g). In the probe test on day 5 for search bias, A+ mice spent less time in the former platform zone than Aw mice ( $F_{1,38} = 12.6$ ,  $p = 0.001$ ) while the T genotype did not affect the search bias ( $p = 0.64$ ). TWD tended to further impair the search bias in the groups with mixed genotypes (AwT+ or A+Tw; Fig. 1h), but overall, the diet main effect was not significant ( $p = 0.10$ ). Altogether, this suggests that TWD exacerbates memory impairment in mice associated with  $\beta$ -amyloid pathology.

#### TWD-induced T2D does not influence $\beta$ -amyloid plaque load but increases the number of neuritic plaques

An obvious question behind the exacerbation of memory impairment of A+ mice by TWD is whether the diet aggravated the brain  $\beta$ -amyloid pathology. This question actually has two components; first, whether the dietary intervention affects the brain  $\beta$ -amyloid load, and second, whether it affects the formation of dystrophic neurites around the  $\beta$ -amyloid plaques, i.e. formation of neuritic plaques that are the most characteristic pathological feature of AD. To this end, we analyzed  $\beta$ -amyloid load in A+ mice in the lateral entorhinal cortex (LEC) and dentate gyrus of hippocampus (HC) (Fig. 1i), the brain sites with the earliest pathological changes in human AD and substantial  $\beta$ -amyloid plaque pathology in the APP<sup>swe</sup>/PS1<sup>dE9</sup> mouse model. One mouse in the A+Tw STD group was removed as an outlier in this analysis to obtain normal distribution of data (Fig. 1j and k). Neither the T+ genotype ( $F_{1,21} = 0.4$ ,  $p = 0.52$ ) nor diet ( $p = 0.17$ ) significantly influenced the  $\beta$ -amyloid load in LEC (Fig. 1j) or in HC (Fig. 1k, T:  $p = 0.50$ , diet:  $p = 0.74$ ). Accordingly, no significant effect by T+ genotype or diet on soluble A $\beta$ 42 (Supplementary Fig. 1a, T:  $F_{1,17} = 0.006$ ,  $p = 0.94$ , diet:  $F_{1,17} = 0.60$ ,  $p = 0.45$ ), A $\beta$ 40

(Supplementary Fig. 1b, T:  $F_{1,17} = 1.0$ ,  $p = 0.32$ , diet:  $F_{1,17} = 3.4$ ,  $p = 0.08$ ), or A $\beta$ 42/40 ratio (Supplementary Fig. 1c, T:  $F_{1,17} = 0.003$ ,  $p = 0.95$ , diet:  $F_{1,17} = 0.37$ ,  $p = 0.55$ ) was found in hippocampal lysates of these mice. Next, we assessed the number of phospho-Tau (AT8)-positive dystrophic neurites around  $\beta$ -amyloid plaques (Fig. 1l). To this end, we counted the number of  $\beta$ -amyloid plaques above the threshold diameter of 9.9  $\mu$ m in three LEC and three HC sections in each mouse, yielding 58–119 plaques per mouse in LEC and 47–84 plaques per mouse in HC. Recent evidence suggests that the number of dystrophic neurites around  $\beta$ -amyloid plaques in transgenic APP mice increases with the plaque diameter [65]. We found a similar relationship between the plaque diameter and the number of dystrophic neurites both in LEC ( $R_{1923} = 0.28$ ,  $p < 0.001$ ) and HC ( $R_{1467} = 0.36$ ,  $p < 0.001$ ) (data not shown). Importantly, the average plaque diameter did not differ between the diet groups either in LEC ( $t_{1921} = 0.48$ ,  $p = 0.63$ ) or in HC ( $t_{1465} = 1.5$ ,  $p = 0.14$ ) (data not shown). However, TWD significantly increased the number of dystrophic neurites around  $\beta$ -amyloid plaques in both LEC ( $F_{1,1919} = 80.3$ ,  $p < 0.001$ ) and HC ( $F_{1,1463} = 6.9$ ,  $p = 0.009$ ), while the T+ genotype had no effect in either LEC ( $p = 0.11$ ) or in HC ( $p = 0.07$ ) (Fig. 1m and n). Furthermore, the area of dystrophic neurites was assessed around  $\beta$ -amyloid plaques in HC with 22C11 antibody, which is another well-established option to detect dystrophic neurites [66] (Supplementary Fig. 1d). The 22C11-positive area around  $\beta$ -amyloid plaques was significantly increased by TWD (Supplementary Fig. 1e, diet:  $F_{1,2697} = 10.24$ ,  $p = 0.001$ ). This increase was evident particularly in the hippocampus of A+Tw mice. Also, a significant interaction effect of diet and genotype was observed (Supplementary Fig. 1e, diet  $\times$  genotype:  $F_{1,2697} = 19.84$ ,  $p < 0.001$ ). We analyzed the correlation between the number of AT8-positive dystrophic neurites/plaque and glucose levels at time 0 min (baseline) and 30 min (peak during GTT) separately in the hippocampus and entorhinal cortex. There was a negative correlation between the number of dystrophic neurites/plaque and glucose levels at time 0 min in hippocampus (Pearson rho  $-0.50$ ,  $p = 0.019$ , Spearman rho  $-0.57$ ,  $p = 0.006$ ). However, we did not detect a similar significant correlation between AT8-positive dystrophic neurites and peak glucose levels in the hippocampus or glucose levels at either time point in the entorhinal cortex. Collectively, the phenotypic and biochemical assessments show that TWD exacerbates memory impairment associated with  $\beta$ -amyloid pathology. However, TWD does not alter total  $\beta$ -amyloid load,  $\beta$ -amyloid peptide ratios or plaque diameter in mouse brain, but instead significantly increases the number of plaque-associated dystrophic neurites.

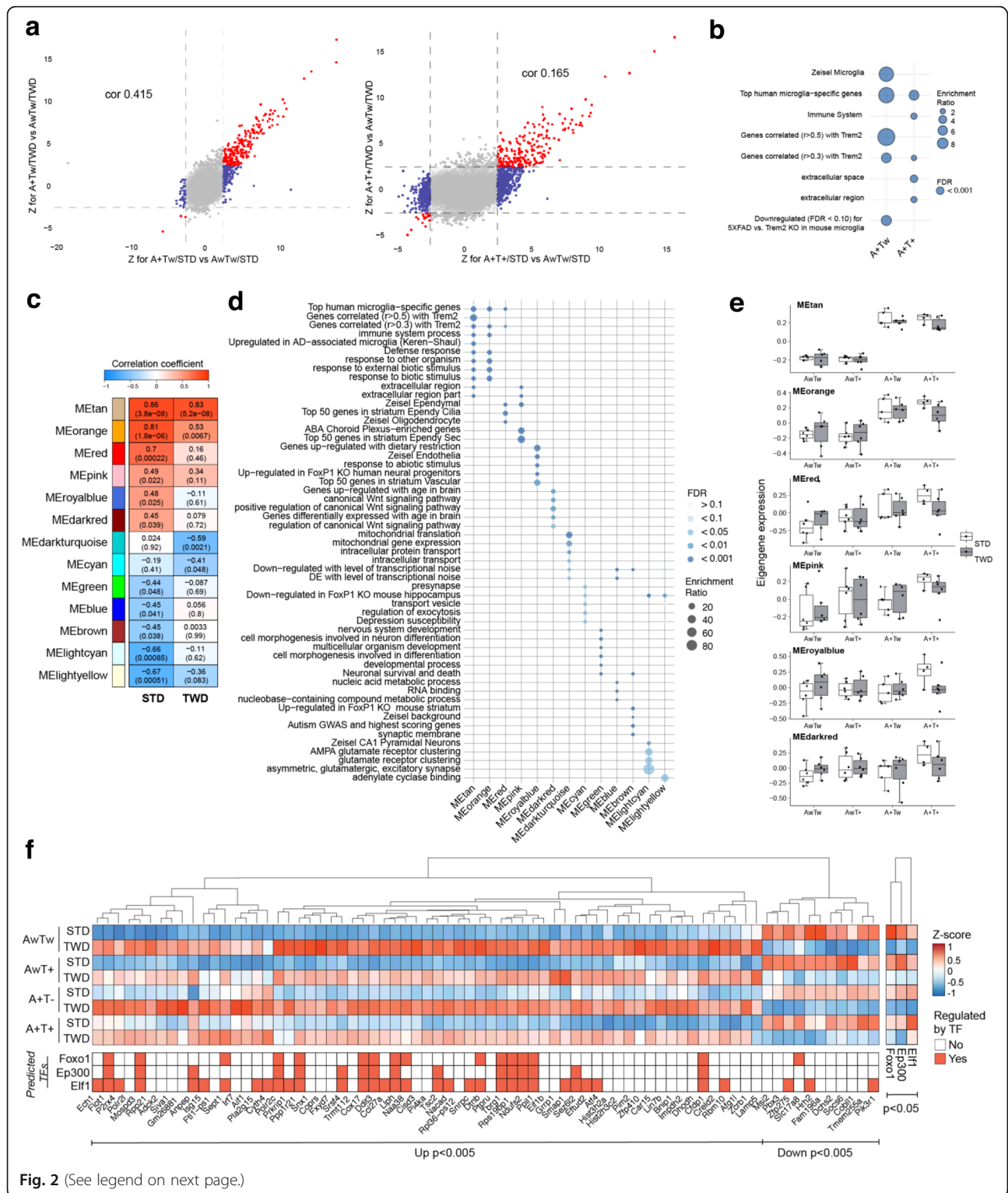
### TWD alters transcriptional response to AD pathology in the hippocampus

To evaluate the impact of TWD on the AD-associated transcriptional response, we performed RNA-sequencing on hippocampal samples from AwTw, AwT+, A+Tw and A+T+ mice on STD or TWD. Assessment of the primary sources of variance in the dataset by principal component analysis (PCA) revealed gradual separation between AwTw, AwT+, A+Tw, and A+T+ mice, with A+T+ showing greatest separation from AwTw mice, suggesting that the combination of  $\beta$ -amyloid and Tau pathologies generates the most potent pathological state (Supplementary Fig. 2b). Separate PCA for mice of each genotype (to dissect diet effects) showed defined separation between STD and TWD samples in all genotypes, suggesting an effect for TWD on the transcriptional landscape of the hippocampus upon both  $\beta$ -amyloid and Tau pathology, as well as in the healthy state (Supplementary Fig. 2c). Surprisingly, almost no genes were differentially expressed (DE; false discovery rate (FDR) < 0.05) in AwT+ mice on both STD (3 up, 1 down) or TWD (1 up, 0 down), when compared to respective AwTw mice (Supplementary Fig. 2d, Supplementary Tables 1 and 2). In turn, we observed 203 DE (199 up, 4 down) genes in A+Tw/STD mice and 173 DE genes (166 up, 7 down) in A+Tw/TWD mice. In accordance with the notion that  $\beta$ -amyloid and Tau pathologies potentiate each other's effects, we observed 338 DE genes (294 up, 44 down) in A+T+/STD mice, but only 177 DE genes (162 up, 15 down) in A+T+/TWD mice. In general, a smaller amount of DE genes was observed in TWD mice when compared to STD mice, which was most evident in A+T+ mice. Comparison of the DE genes between STD and TWD mice for each genotype show a large overlap in genes, with unique DE genes mainly observed in STD mice (Supplementary Fig. 2e), suggesting a similar but less potent response in TWD mice when compared to STD mice. To further compare the transcriptional response between STD and TWD mice, we correlated DE analysis Z-statistic values for STD and TWD mice for each genotype. A strong positive correlation can be considered a highly similar transcriptional response. This analysis revealed only modest correlations (AwT+,  $\text{cor} = -0.309$  (data not shown); A+Tw,  $\text{cor} = 0.415$ ; A+T+,  $\text{cor} = 0.165$ , Fig. 2a), supporting the notion that TWD mice display an impaired transcriptional response to AD-related pathologies. Next, we performed enrichment analyses of DE genes (Supplementary Table 3) using a curated collection of both public gene sets (e.g., GO and MSigDB) and self-curated gene set collections (Methods). Consistent for both A+Tw and A+T+ mice, the top enrichment term for upregulated genes was "Top human microglia-specific genes", irrespective of diet, highlighting the importance of

microglia responding to  $\beta$ -amyloid pathology. Interestingly, a significant enrichment for synaptic function-associated terms (e.g. "chemical synaptic transmission"  $p = 6.7 \times 10^{-03}$ ) was only observed for genes downregulated in A+T+/TWD mice. Enrichment analysis of genes showing an impaired response in Z-statistic value comparisons in mice with A+/T- or A+T+ background upon TWD as compared to STD mice (Fig. 2a, blue points:  $Z > 2.5$  or  $< -2.5$  in STD, but not in TWD) indicated enrichment for microglia-specific terms (e.g. "Top human microglia-specific genes", "Genes correlated with Trem2"), suggesting that TWD to an extent impairs the transcriptional response of microglia (Fig. 2b) (Supplementary Table 4). Expression profiles of genes displaying a discordant response revealed that the majority of genes were either up- or downregulated already in AwTw mice, showing only minor changes in relation to  $\beta$ -amyloid and/or Tau pathology (Supplementary Fig. 3a). This could suggest that TWD locks microglia to a type of intermediate state. Intriguingly, enrichment analysis of genes showing enhanced response in Z-statistic value comparisons in mice with A+/T- or A+T+ background upon TWD as compared to STD mice (Fig. 2a, points:  $Z > 2.5$  or  $< -2.5$  in TWD, but not in STD) also highlighted terms related to "immune/defense response", "positive regulation of cytokine production", "MHC protein complex" (Supplementary Fig. 3b). Taken together, these results suggest a large range of transcriptional changes due to TWD, which potentially alter the response of microglia and neurons to  $\beta$ -amyloid and/or Tau pathology as compared to STD mice.

### TWD diminishes specific $\beta$ -amyloid and tau pathology-associated microglial gene expression signatures

To further identify AD pathology-associated molecular networks that may be selectively affected by TWD in mouse brains, we performed consensus weighted gene co-expression network analyses (WGCNA [52]). Our consensus WGCNA analysis identified 28 co-expression modules (Supplementary Table 5; Fig. 2c). By relating the module eigengene (a representative vector for the genes in a module, see methods), [52] to genotype, we identified six modules significantly positively associated and seven modules significantly negatively associated with genotype in either STD or TWD mice (Fig. 2c). A positive association can be considered as an increase in the expression of module genes in response to A+ and/or T+ background, and vice versa for negative association. A weaker association for the majority of the positively and negatively related modules in TWD mice was detected (Fig. 2c). Conversely, two negatively associated modules (MEdarkturquoise, MECyan) showed a weaker association in STD mice (Fig. 2c). Comparison of the relations between STD and TWD network modules



(See figure on previous page.)

**Fig. 2** Transcriptomic and co-expression network analysis reveal impaired microglial response to AD-related pathology. **a** Transcriptome-wide response comparison of STD and TWD mice to A+ and A+T+ background. Plots show Z-statistics derived from DE analysis for A+Tw/STD vs. AwTw/STD (x-axis) and A+T+/TWD vs. AwT+/TWD (y-axis) (left) and A+T+/STD vs. AwT+/STD (x-axis) and A+T+/TWD vs. AwT+/TWD (y-axis) (right). Points (genes) showing concordant response in STD and TWD cases are indicated in red, and discordant response for TWD as compared to STD, in blue. Genome-wide correlations of Z statistics and the corresponding correlation values are indicated on the top of each panel. **b** Enrichment analysis of genes showing discordant response to A+ or A+T+ background in TWD mice as compared to STD mice (blue dots in a). Enrichment ratio = number of observed divided by the number of expected genes. **c** WGCNA modules significantly associated to genotype in either STD or TWD mice. The color and value in the box represent correlation coefficient value. The value in parentheses represents corresponding correlation *p*-value. **d** Enrichment analysis for WGCNA module genes. Color indicates FDR value and size enrichment ratio. **e** Box plots representing eigengene values for modules positively associated with genotype. Points represent eigengene values for each mouse in that group. Box plots show the median, 25th and 75th percentiles, error bars show 1.5 interquartile ranges. **f** Z-score value heatmap of DE genes for STD vs. TWD mice with FDR < 0.005 and enriched transcription factors (TFs) with FDR < 0.05. *n* = 4–6 mice/group. AwTw = wild-type, AwT+ = Tau P301L, A+Tw = APP<sup>swe</sup>/PS1<sup>dE9</sup>, A+T+ = APP<sup>swe</sup>/PS1<sup>dE9</sup> x Tau P301L

similarly revealed a loss in network preservation upon TWD as compared to the STD network, largely for positively associated modules, especially the MEdarkred module (Supplementary Fig. 3c).

Cell type enrichment analysis of the network modules revealed a significant enrichment for neuronal and astrocytic markers for negatively regulated modules, and for microglial and endothelial cell markers in positively correlated modules (Supplementary Fig. 3d). Accordingly, modules that negatively correlated with genotype were significantly enriched for neuron-related terms (Fig. 2d; Supplementary Table 6). In turn, top positively correlated modules were significantly enriched for “Top Human Microglia-Specific Genes”, and more specifically “Immune Response”, “Genes Correlated with Trem2”, and genes “Upregulated in AD-associated Microglia (Keren-Shaul et al., 2017)” (Fig. 2d). This suggests that the top identified positively associated modules recapitulate a microglial Trem2-driven DAM response, which is partially impaired upon TWD. MEdarkred, which had a poor preservation between the STD and TWD networks, was significantly enriched in genes related to the Wnt signaling pathway. Previously, it was shown that down-regulation or knock-out of Trem2 in microglia results in reduced Akt S473 and Gsk3 $\beta$  S9 phosphorylation, resulting in  $\beta$ -catenin degradation and impaired Wnt/ $\beta$ -catenin [67]. Observation of expression levels for genes associated with Trem2/DAM/Wnt signaling terms further highlight the imbalance induced by TWD, with partial enhanced and suppressed expression of associated genes (Supplementary Fig. 4). These results suggest that TWD in mice potentially alters microglial functionality downstream of Trem2 signaling, thus resulting in the observed partial transcriptional response when compared to STD mice.

To assess whether any modules associated with Tau pathology,  $\beta$ -amyloid pathology or the combination of both, we plotted eigengene expression levels for each genotype and diet (Fig. 2e, Supplementary Fig. 3e). The most evident pathology-dependent alterations were

observed in the top two positively associated modules, MEtan and MEorange, where an increase in eigengene expression was driven primarily by the presence of  $\beta$ -amyloid pathology. In turn, MEdarkturquoise, MEgreen, MELightyellow, MEblue, and MELightcyan, and MEred and MEpink modules showed a more linear change in expression (in order: AwTw, AwT+, A+Tw, A+T+), with the greatest decrease or increase in A+T+ mice when compared to AwTw mice. Interestingly, MERoyalblue and MEdarkred modules showed only modest or no changes in expression in AwT+ or A+Tw mice, but an increase in expression in A+T+ mice. This suggests that in some cases  $\beta$ -amyloid and Tau cooperate to cause specific transcriptional alterations in mouse brain, which is in line with recent findings [68]. Overall, our network analysis reveals a strong transcriptional response to  $\beta$ -amyloid pathology and combined  $\beta$ -amyloid and Tau pathologies in genes predominantly expressed in microglia and associated with microglia-specific biological terms. Specifically, a Trem2-driven DAM type profile was recapitulated, and this was partially impaired in TWD mice, potentially due to altered downstream signaling of Trem2.

#### TWD induces aberrant expression of disease-associated microglia signature genes in mouse hippocampus

As TWD was found to change the transcriptional landscape in mouse hippocampus in WT (AwTw) and transgenic mice (AwT+, A+Tw, A+T+), resulting in an altered basal state and response to  $\beta$ -amyloid and Tau pathology, we next concentrated on the genes that were altered by the diet irrespective of genotype to pin-point potential key TWD-associated pathways. DE analysis for TWD mice vs. STD mice revealed 4428 DE genes (2698 up, 1730 down, Fig. 2f; Supplementary Table 7), enriched for terms related to ribosomes, mitochondria (e.g. “mitochondrial protein complex”), and genes up-/downregulated in AD-/ALS-associated microglia (“Up-regulated in AD-associated microglia [32], “Up-regulated in Stage2 vs. Stage1 disease-associated microglia”)

(Supplementary Table 8). Given that our genotype and diet DE analysis and network analysis suggested that TWD alters the previously described DAM response, we examined the overlap between TWD DE genes and DAM genes ([32], genes with  $FDR < 0.01$  and  $FC > 3$  or  $< -3$ ). This analysis revealed an overlap of 132 genes with top DE hits, such as *Pik3r1* ( $FDR = 0.004$ ,  $\text{Log}_2FC = -0.40$ ), *Tyrobp* ( $FDR = 0.006$ ,  $\text{Log}_2FC = 0.37$ ), and *Trem2* ( $FDR = 0.008$ ,  $\text{Log}_2FC = 0.29$ ). The expressional changes of *Pik3r1*, *Trem2*, and *Tyrobp* detected by RNA-sequencing were confirmed using conventional qPCR (Supplementary Fig. 5a-b). Despite observing a general lack of transcriptional response associated with *Trem2* correlated genes, we observed an increase in both *Trem2* and *Tyrobp* expression levels. However, the expression of *Pik3r1*, a gene encoding PI3K regulatory subunit 1 and directly acting downstream of *Trem2*, was decreased. This finding highlights *Pik3r1* as a potentially important candidate in conveying the observed TWD effects, given the importance of the PI3K-mediated insulin signaling in the brain, the role of the *Trem2*-PI3K-Akt pathway in DAM activation, and the observed alterations in *Trem2*- and Wnt signaling pathways in our WGCNA analysis. The altered expression levels for PI3K-Akt pathway-associated genes supports this notion, as most of the genes show a similar reduction in expression upon TWD (Supplementary Fig. 4b). Lastly, as TWD causes a large scale of transcriptomic effects, we sought to determine the transcription factors potentially regulating the observed top DE genes ( $p < 0.005$ ). Enrichment for three significantly differentially expressed transcription factors, *Foxo1*, *Ep300*, and *Elf1* was identified (Fig. 2f).

#### TWD leads to decreased Akt and increased Gsk3 $\beta$ activation in hippocampus

Since analysis of the RNA-sequencing data highlighted decreased expression levels of *Pik3r1*, the gene encoding p85 $\alpha$  subunit of PI3K, and several genes associated with the PI3K-Akt pathway, in hippocampus of mice with TWD as compared to STD, we next assessed whether there are alterations in well-known downstream targets in PI3K-Akt-Gsk3 $\beta$ -Tau pathway. We analyzed hippocampal protein lysates using Western blot and found that phosphorylation of S473 in Akt1 kinase, a residue regulating Akt1 activation, was significantly decreased in TWD mice as compared to STD mice ( $F_{1,38} = 30$ ,  $p < 0.001$ , Fig. 3a). This was an expected finding, considering the decreased p85 $\alpha$  expression. In line with this, phosphorylation of the corresponding S474 site in Akt2 ( $F_{1,38} = 9.9$ ,  $p = 0.003$ , Fig. 3b) and of another activating site, T308/309/305 in Akt1/2/3, respectively, ( $F_{1,38} = 28.9$ ,  $p < 0.001$ , Fig. 3c) were significantly decreased in the hippocampus of TWD mice as compared to STD mice. Furthermore, Akt-mediated phosphorylation of the

inhibitory S9 residue in Gsk3 $\beta$ , a well-characterized Tau-kinase, was significantly decreased in mice on TWD as compared to STD ( $F_{1,38} = 14.3$ ,  $p < 0.001$ , Fig. 3d), suggesting increased Gsk3 $\beta$  activity. However, no diet effect was observed on Tau phosphorylation between the TWD and STD mice ( $F_{1,37} = 0.67$ ,  $p = 0.42$ ), while Tau phosphorylation was significantly reduced in mice with T+ genotype (Supplementary Fig. 1f,  $F_{1,37} = 48$ ,  $p < 0.001$ ). The typical 64-kDa band [69] present above the endogenous mouse Tau bands in T+ mice (P301L over-expressing human Tau) was included into the quantification. However, excluding the 64-kDa band from the analysis does not change the result. As expected, total Tau levels were significantly increased in T+ as compared Tw mice (Supplementary Fig. 1f,  $F_{1,41} = 141$ ,  $p < 0.001$ ). The diet also had a significant effect on total Tau levels ( $F_{1,41} = 10.8$ ,  $p = 0.002$ ). As previously described, hyperphosphorylated, aggregated Tau becomes insoluble, which might explain why increased Tau phosphorylation was not detected in hippocampal homogenates in this analysis. In contrast, IHC analysis showed that TWD significantly exacerbated dystrophic neurite i.e. phosphorylated Tau pathology in both A + Tw and A + T+ mice in the vicinity of  $\beta$ -amyloid plaques (HC and LEC, Fig. 11-m).

Since energy metabolism and PI3K-Akt signaling are known to regulate autophagy, protein levels of well-known autophagy markers p62 and LC3B were next assessed in hippocampal lysates. Levels of p62 were significantly increased in TWD mice as compared to STD mice (Fig. 3e,  $F_{1,38} = 6.9$ ,  $p = 0.012$ ), suggesting that TWD decreases autophagy. This was unexpected, since impaired activation of PI3K-Akt pathway has been shown to lead to decreased levels of p62 [70, 71] reflecting enhanced autophagic degradation. LC3B detection revealed increased levels of cytosolic LC3BI form and no membrane-bound lipidated LC3BII form in TWD mice as compared to STD mice (Fig. 3e,  $F_{1,38} = 6.3$ ,  $p = 0.016$ ), further suggesting decreased autophagy.

Hippocampus is in a central role in processes related to learning and memory. Thus, we next analyzed whether the results of the behavioral tests correlated with any biochemical assessments in the hippocampal lysates. Higher body weight at age of 12 months (W12) and higher weight gain (WG) between 5 and 12 months negatively correlated with phosphorylation of Akt1 S473 (W12:  $R = -0.417$ ,  $p < 0.01$  and WG:  $R = -0.453$ ,  $p < 0.01$ ), Akt2 S474 (W12:  $R = -0.373$ ,  $p < 0.01$  and WG:  $R = -0.373$ ,  $p < 0.01$ ) and Gsk3 $\beta$  S9 (W12:  $R = -0.292$ ,  $p < 0.05$  and WG:  $R = -0.331$ ,  $p < 0.05$ ). However, no correlation between peripheral glucose intolerance and Akt/Gsk3 $\beta$  phosphorylation status was found. Interestingly, mean latency time to find the hidden platform in the acquisition phase of Morris swim task revealed a strong



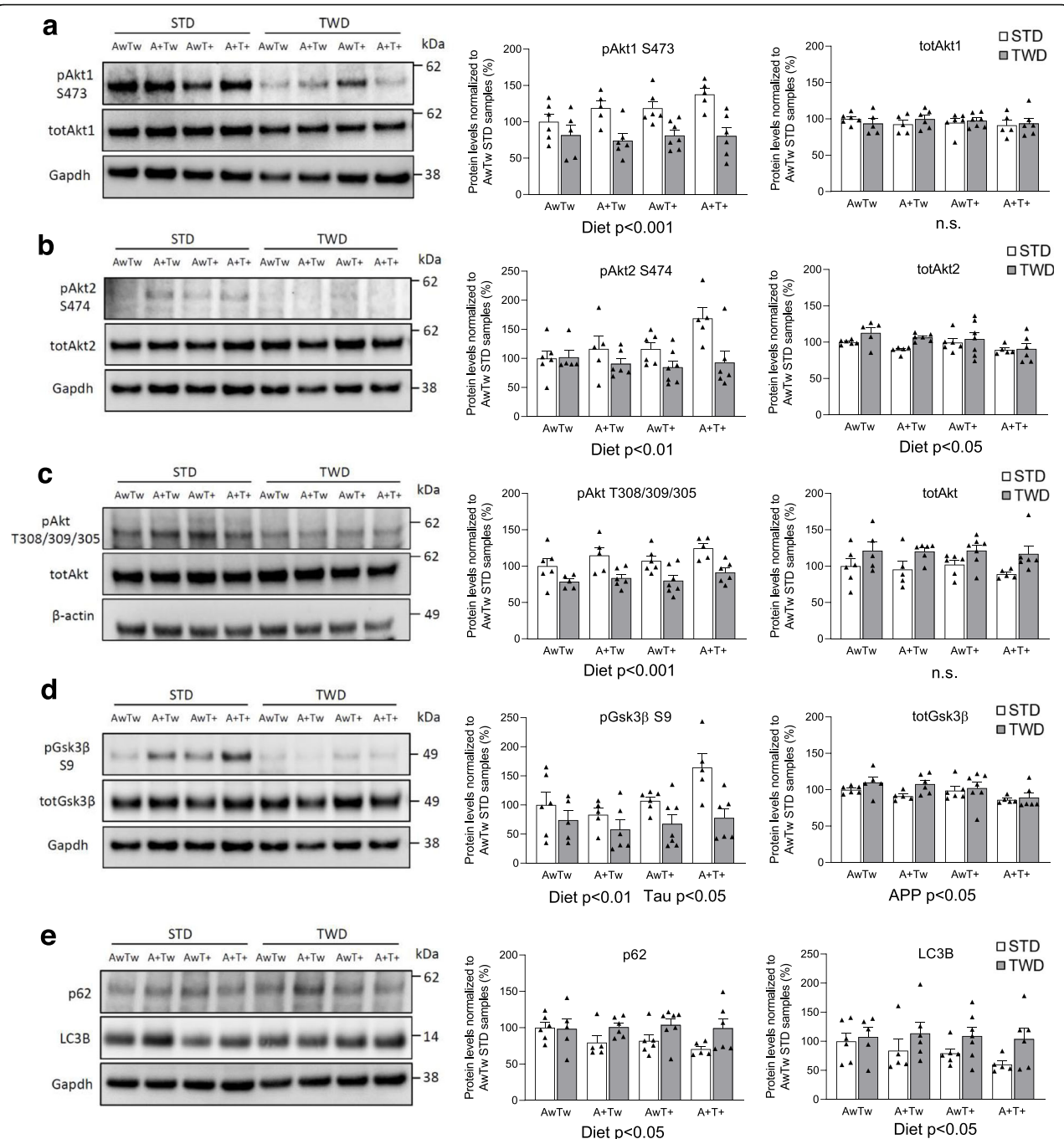


**Fig. 3** TWD induces impaired Akt-Gsk3 $\beta$  signaling in the brain. **a** Western blot analysis of hippocampal lysates showing decreased phosphorylation of S473 in Akt1 in mice with TWD as compared to STD ( $p < 0.001$ ). Diet had no effect on total Akt1 levels. **b** Similarly, phosphorylation of S474 in Akt2 is decreased in mice with TWD as compared to STD ( $p < 0.01$ ). Diet had a minor, but statistically significant effect on total Akt2 levels ( $p < 0.05$ ). **c** Also, phosphorylation of T308/309/305 residue in Akt1/2/3, respectively, was significantly decreased in mice with TWD as compared to STD ( $p < 0.001$ ). Total Akt1/2/3 levels showed no significant changes. **d** Phosphorylation of Gsk3 $\beta$  at the inhibitory S9 residue was significantly decreased in mice with TWD as compared to mice with STD ( $p < 0.01$ ). A+ transgene (APPswe/PS1dE9) increased slightly, but significantly Gsk3 $\beta$  S9 phosphorylation ( $p < 0.05$ ) as well as total Gsk3 $\beta$  levels ( $p < 0.05$ ). **e** A representative Western blot image and quantification of hippocampal lysates showing increased levels of the autophagy markers p62 and LC3B in TWD mice as compared to STD mice ( $p < 0.05$ ). Phosphorylated protein levels were normalized to their respective total protein levels in cell lysates and total protein levels were normalized to Gapdh or  $\beta$ -actin. All results are shown as mean + SEM,  $n = 5-7$  mice/group, Two-way ANOVA. AwTw = wild-type, AwT+ = Tau P301L, A+Tw = APPswe/PS1dE9, A+T+ = APPswe/PS1dE9 x Tau P301L

negative correlation with phosphorylation of Akt1 S473 ( $R = -0.355$ ,  $p < 0.016$ ), Akt2 S474 ( $R = -0.286$ ,  $p = 0.054$ ), and Gsk3 $\beta$  S9 ( $R = -0.353$ ,  $p < 0.05$ ), suggesting that the stronger the Akt/Gsk3 $\beta$  signaling, the faster the mice find the platform. However, spontaneous movement activity did not correlate with Akt or Gsk3 $\beta$  phosphorylation. Altogether, these results strongly suggest that decreased *Pik3r1* expression upon TWD coincides with significantly decreased activity of Akt1/2 (both S473/474 and T308/309/305 catalytic sites) and increased activity of Gsk3 $\beta$ . Furthermore, TWD exacerbates dystrophic neurite pathology in both A+Tw and A+T+ mice in the vicinity of  $\beta$ -amyloid plaques (HC and LEC, Fig. 11-n).

#### TWD reduces clustering of microglia around $\beta$ -amyloid plaques in mice

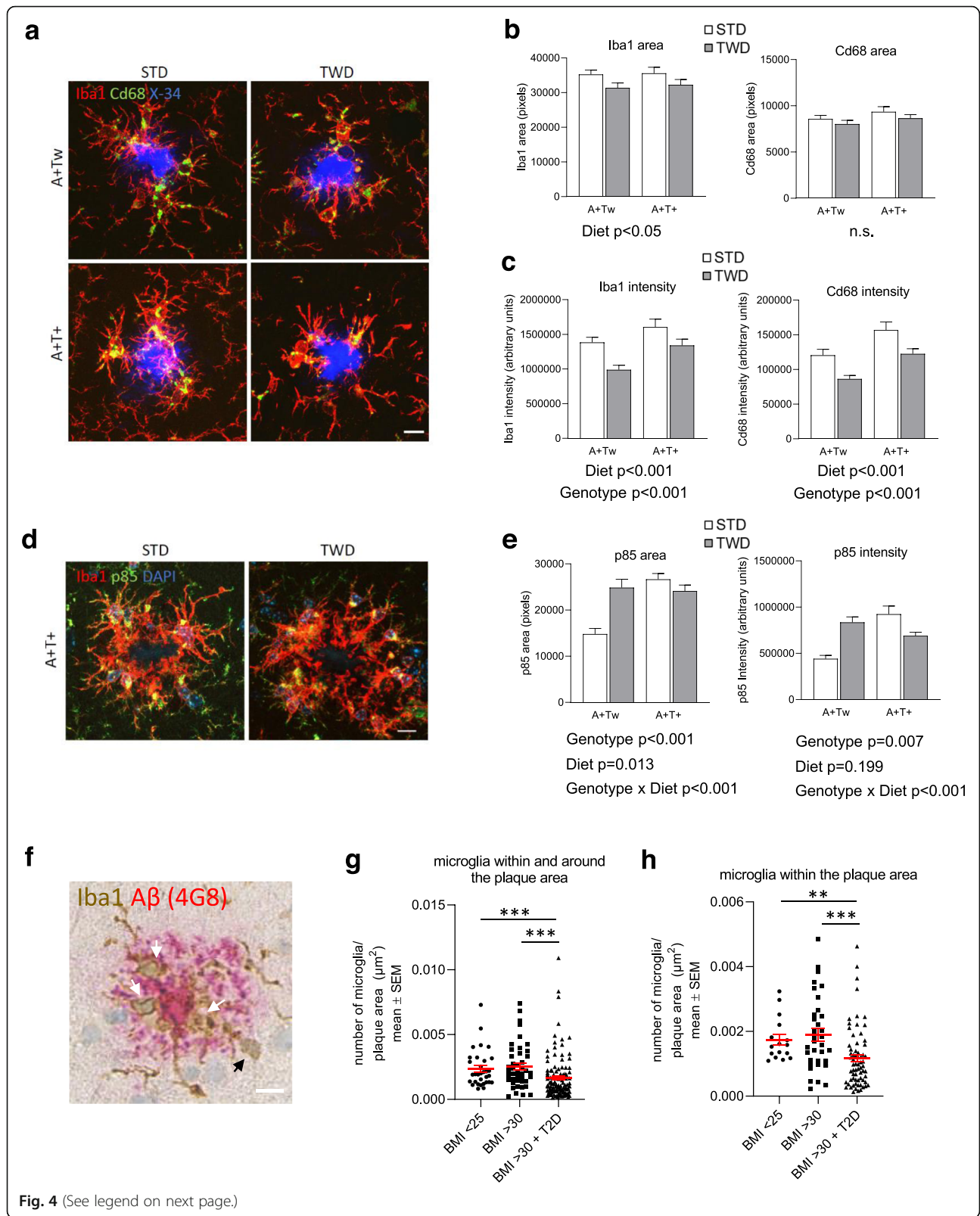
Since RNA-sequencing data also suggested that TWD leads to altered Trem2-signaling and general transcriptional response of microglia, we next assessed if TWD affected microglia-related pathology around  $\beta$ -amyloid plaques in mouse and human IHC samples. Hippocampal sections of A+Tw and A+T+ mice were triple-stained with anti-Iba1 (microglia), anti-Cd68 (lysosomal marker expressed in activated microglia) and X-34 ( $\beta$ -amyloid plaque) to assess microglia clustering and lysosomal activity around plaques. Iba1-positive area within 30  $\mu$ m from the plaque was found to decrease in TWD as compared to STD mice (Fig. 4a and b, diet  $p < 0.05$ ). No diet effect on Cd68-positive area was observed. However, significant reduction of both Iba1 and Cd68 intensities were detected in mice fed with TWD as compared to mice fed with STD (Fig. 4c, diet  $p < 0.001$ ), suggesting that the number of microglia and lysosomal activity around plaques is reduced. Also, T+ genotype, on top of the A+ background, significantly increased both Iba1 and Cd68 intensity (Fig. 4c,  $p < 0.001$ ), suggesting that Tau pathology further potentiates microglia activation in A+ mice. Microglia morphology around  $\beta$ -amyloid plaques was assessed to address the possibility that changes in cell morphology could explain the differences in Iba1-positive area. No differences were observed in the number of process endpoints or process length between the genotype or diet groups (Supplementary Fig. 5c). In addition to IHC analysis, expression levels of Iba1, Cd68 and a subset of other microglia-specific genes were analyzed in all genotype and diet groups using hippocampal RNA-seq data (Supplementary Fig. 5d). Only Iba1 showed a statistically significant increase in the expression levels in AwTw mice with TWD as compared to AwTw mice with STD ( $p = 0.037$ ). None of the other genes showed a statistically significant diet effect in any of the genotypes after adjusting the  $p$ -values for multiple comparison. This result suggests that diet may have

divergent effects on microglia in Aw mice as compared to A+ mice.

Next, we wanted to assess whether the decrease of p85 $\alpha$  expression observed at the transcriptional level could also be detected specifically in microglia around  $\beta$ -amyloid plaques in IHC samples. Hippocampal sections of mice with A+Tw and A+T+ genotypes were triple stained with anti-Iba1, anti-p85 $\alpha$  and DAPI to assess p85 $\alpha$  in microglial cells. Plaque-associated microglia were identified by the typical clustering pattern of Iba1 immunopositive microglia around the  $\beta$ -amyloid plaques (Fig. 4a and d). The analysis revealed a significant genotype  $\times$  diet interaction on both p85 $\alpha$  area and intensity (Fig. 4e, genotype  $\times$  diet,  $F_{1,247} = 15.2$ ,  $p < 0.001$ ). In A+Tw mice, TWD increased the levels of p85 $\alpha$  in microglia surrounding the  $\beta$ -amyloid plaques. The T+ genotype also increased p85 $\alpha$  levels in the microglia around  $\beta$ -amyloid plaques (Fig. 4e, T+ genotype,  $F_{1,247} = 15.9$ ,  $p < 0.001$  for p85 $\alpha$  area and  $F_{1,247} = 7.2$ ,  $p = 0.008$  for p85 $\alpha$  intensity). However, in contrast to A+Tw on TWD and A+T+ mice on STD, TWD induced a significant reduction in the levels of p85 in plaque-associated microglia in A+T+ mice. In conclusion, these data indicate that TWD reduces clustering of microglia around the  $\beta$ -amyloid plaques in A+Tw and A+T+ mice, which could be linked to the altered expression of p85 $\alpha$  in the microglia.

#### Metabolic phenotype affects microglia clustering around $\beta$ -amyloid plaques in probable iNPH patients with $\beta$ -amyloid pathology

To assess the effect of the metabolic phenotype on microglia in humans, we analyzed the extent of microglia clustering around  $\beta$ -amyloid plaques (Fig. 4f) in frontal cortical biopsies obtained from living patients with probable iNPH (Table 1). Subjects were divided into three groups: normal weight individuals (BMI  $< 25$ ), obese individuals (BMI  $> 30$ ), and obese individuals with T2D diagnosis (BMI  $> 30$  + T2D). In accordance with our findings in TWD-fed mice, we observed a statistically significant decrease in the number of microglia around  $\beta$ -amyloid plaques in obese individuals with T2D as compared to both normal weight and obese individuals without T2D, when assessing microglia both around and within the plaque area ( $p < 0.001$ ) (Fig. 4g) as well as microglia only within the plaque area ( $p < 0.001$ ) (Fig. 4h). No difference was observed in the number of plaque-associated microglia between BMI  $< 25$  and BMI  $> 30$  groups. Furthermore, the number of microglia distant from the plaques was not different between any of the groups (data not shown). Thus, our results indicate that T2D, not obesity, reduces microglia clustering around  $\beta$ -amyloid plaques in the frontal cortical biopsies of probable iNPH patients.



(See figure on previous page.)

**Fig. 4** TWD and T2D alter microglial response to  $\beta$ -amyloid plaques in AD mice and human brain biopsies. **a** Representative immunofluorescence images of  $\beta$ -amyloid plaques stained with X-34 (blue) surrounded by Iba1 positive microglia (red) and lysosomes stained with Cd68 (green) from A+Tw and A+T+ mice from both STD and TWD groups. Scale bar 10  $\mu$ m. **b** Quantification revealed that TWD significantly ( $p < 0.05$ ) decreased Iba1 positive area (pixels) as compared to STD in both A+Tw and A+T+ mice, while diet showed no effect on Cd68 positive area. **c** Also, intensity of both Iba1 and Cd68 (arbitrary units) was significantly decreased ( $p < 0.001$ , both) in mice with TWD as compared to STD in both genotypes. Furthermore, T+ transgene (Tau P301L) significantly increased both Iba1 and Cd68 intensity ( $p < 0.001$ , both). **d** Representative immunofluorescence images of Iba1 positive microglia (red) and p85 $\alpha$  staining (green) around  $\beta$ -amyloid plaques in hippocampus of A+T+ mice from both STD and TWD groups. Scale bar 10  $\mu$ m. **e** Quantification of p85 $\alpha$  revealed statistically significant genotype  $\times$  diet interaction ( $p < 0.001$ ) in both p85 $\alpha$  area and p85 $\alpha$  intensity. T+ transgene significantly increased both p85 $\alpha$  area ( $p < 0.001$ ) and p85 $\alpha$  intensity ( $p = 0.007$ ), while diet had opposing effects on p85 $\alpha$  depending on the genotype. **a–e** results are shown as mean  $\pm$  SEM,  $n = 5–6$  mice/group, Two-Way ANOVA. **f** Representative image of frontal cortex biopsy sample from probable iNPH subject co-stained for IBA1 (brown) and  $\beta$ -amyloid (red). White arrows denote microglia within the plaque area, and black arrow denotes microglia around the plaque area. Scale bar 10  $\mu$ m. **g** Quantification of IBA1-positive microglia within and around the  $\beta$ -amyloid plaque. **h** Quantification of IBA1-positive microglia within the plaque area. **g–h**; results are shown as mean  $\pm$  SEM,  $n = 3–5$  subjects/group. AwTw = wild-type, AwT+ = Tau P301L, A+Tw = APPswe/PS1dE9, A+T+ = APPswe/PS1dE9  $\times$  Tau P301L

### Modulation of PI3K-Akt signaling pathway affects phagocytosis and proinflammatory response in mouse microglia

Since TWD exacerbated dystrophic neurite pathology, reduced the clustering of microglia around  $\beta$ -amyloid plaques, and decreased the expression of *Pik3r1* in the hippocampus of A+Tw and A+T+ mice as compared to STD mice with the same genetic backgrounds, we next examined the microglia-specific molecular mechanisms underlying these observations. PI3K is a heterodimeric enzyme composed of the catalytic p110 subunit and the regulatory p85 subunit, which catalyzes the phosphorylation of PI(4,5)P<sub>2</sub> to the lipid second messenger PI(3,4,5)P<sub>3</sub> [24]. *Pik3r1* is abundantly expressed in mouse microglia [62] and it encodes three regulatory isoforms of PI3K (p85 $\alpha$ , p55 $\alpha$  and p50 $\alpha$ ), which are produced through alternative splicing [72]. To modulate PI3K-Akt signaling and to model the subsequent effects of decreased *Pik3r1* expression in mouse BV2 and neonatal primary microglia upon basal and LPS-induced stress conditions, we used the well-established PI3K inhibitor LY294002 and studied the effects on autophagosomal activity (the ratio of LC3BII/I), mitogen-activated protein kinase kinase (Mek)/extracellular signal-regulated kinase (Erk) pathway, apoptosis, and phagocytic uptake (Fig. 5a–f). The treatment of BV2 cells with LY294002 showed an expected dose-dependent decrease in the phosphorylation status of S473 in Akt (pAkt) in both normal and LPS-induced stress conditions (Fig. 5a and b), reflecting decreased Akt activity. LPS treatment alone significantly increased the levels of pAkt in BV2 cells as compared to untreated cells, which is consistent with our previous results [73]. In parallel with the reduced activity of Akt, the ratio of the autophagosomal marker LC3BII/I was increased in a dose-dependent manner as expected, particularly in the BV2 cells treated with both LPS and LY294002 (Fig. 5a–d and Supplementary Fig. 6a–c). Conversely, the phosphorylation status of Erk1 and 2 (pErk1 and 2) in the activating Y204 site decreased

in a dose-dependent manner in LY294002 samples, while the levels of active caspase-3 and p85 $\alpha$  were unchanged in the BV2 cells treated with both LPS and LY294002 (Supplementary Fig. 6d–j).

Next, live cell imaging of BV2 and primary microglia treated with LY294002 revealed a dose-dependent decrease in the phagocytic uptake of pHrodo-labeled bioparticles (Fig. 5e and f). Moreover, primary microglia isolated from neonatal Akt2 knock-out (Akt2 KO) mice also showed a significant decrease in the phagocytic uptake of pHrodo-labeled bioparticles as compared to WT microglia (Fig. 5f). The treatment of Akt2 KO microglia with LY294002 further decreased the phagocytic uptake of bioparticles as compared to untreated Akt2 KO microglia. Akt2 KO microglia cultures showed reduced levels of secreted Tnf- $\alpha$ , Il6 and nitric oxide (NO) in the culture medium as compared to the WT microglia cultures in response to LPS treatment (Fig. 5g). Altogether, these results suggest that the inhibition of PI3K-Akt signaling by using pharmacological (LY294002) or genetic (Akt2 KO mouse model) approaches significantly decreases the phagocytic uptake affects the autophagic and Erk kinase activity, and dampens the production of proinflammatory cytokines and NO upon LPS-induced stress in mouse microglia.

### Ligand-induced activation of Trem2/Dap12 upon the inhibition of PI3K-Akt signaling enhances the activation of spleen tyrosine kinase in mouse microglia

PI3K plays a central role in the Trem2/Dap12-mediated signaling in mouse macrophages and osteoclasts upon ligand-induced activation, resulting in alterations in Erk kinase activity, mobilization of calcium, reorganization of actin, and apoptosis [74]. Importantly, the same study showed that inhibition of PI3K prevented recruitment of p85 $\alpha$  and spleen tyrosine kinase (Syk kinase) to Dap12. This is an intriguing finding given the fact that upon ligand binding to Trem2, the tyrosine residues within ITAM domain of Dap12 are phosphorylated, which leads

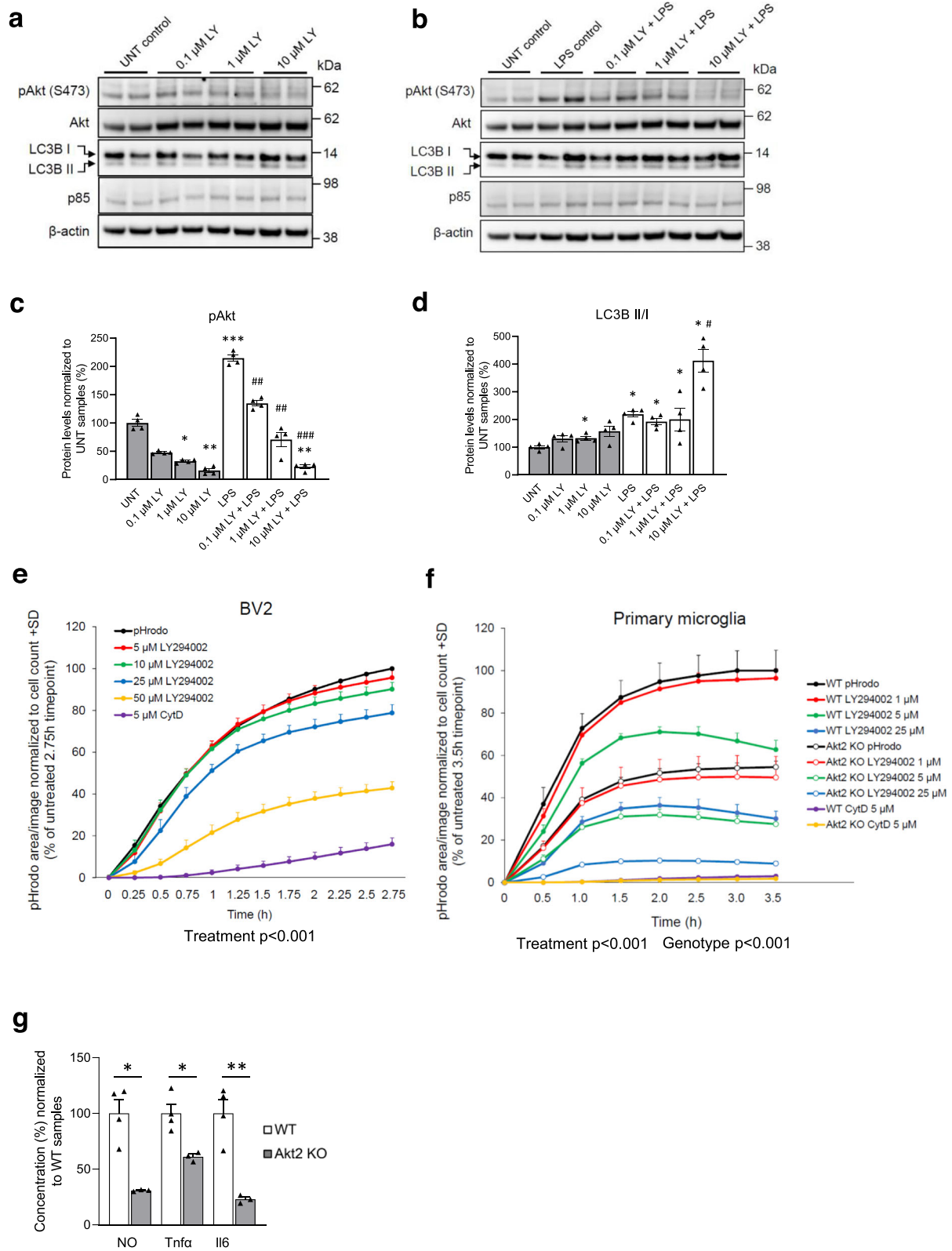


**Fig. 5** (See legend on next page.)

(See figure on previous page.)

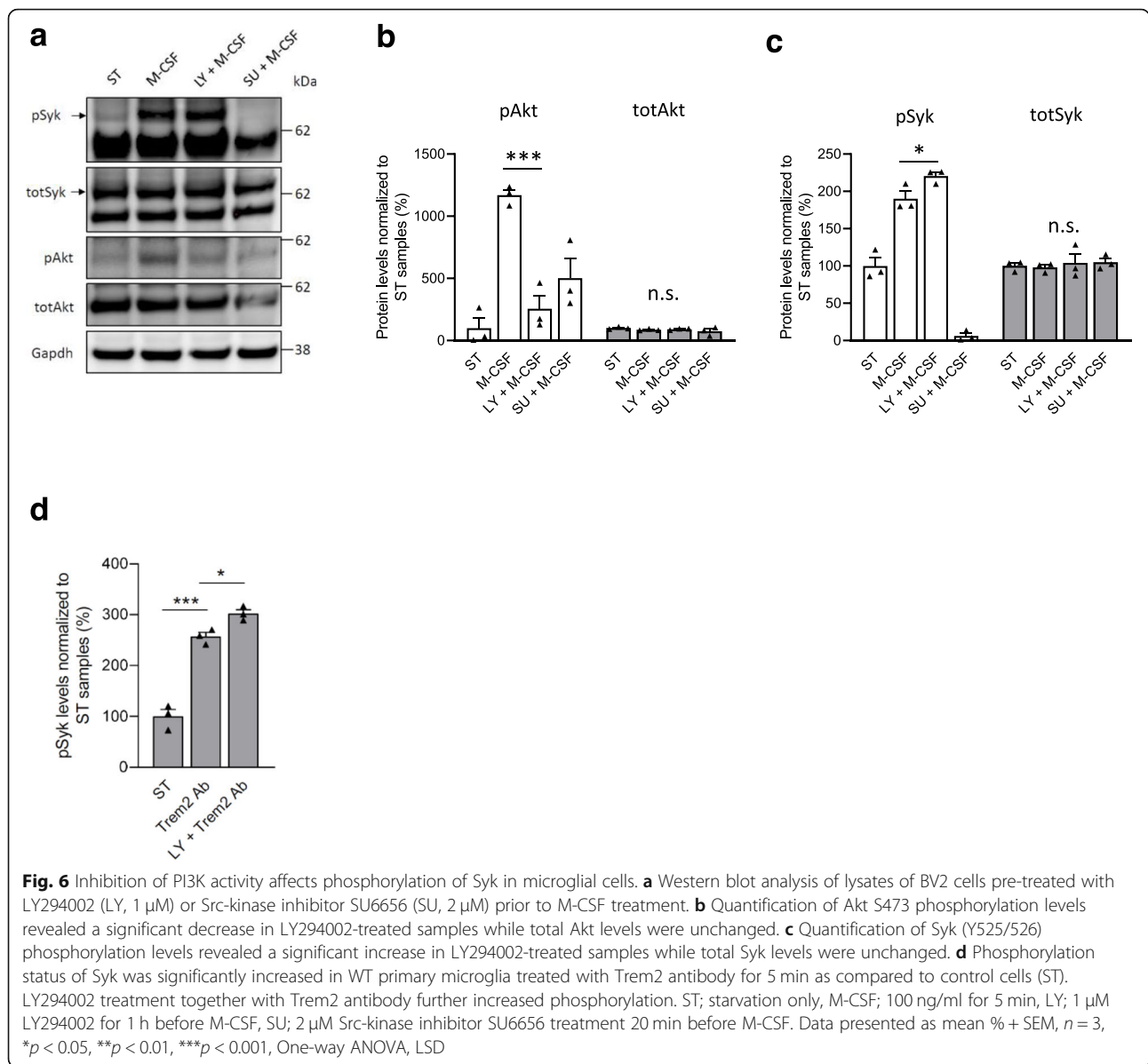
**Fig. 5** Modulation of PI3K-Akt pathway affects autophagic and phagocytic activity as well as inflammatory response in microglial cells. **a** A representative Western blot image of lysates of BV2 cells treated with LY294002 (LY) (0.1  $\mu$ M – 10  $\mu$ M), and **b** with LY294002 together with LPS. **c** Quantification revealed that LY294002 decreased Akt S473 phosphorylation levels dose-dependently in cells treated with LY294002 and together with LPS and LY294002. **d** Quantification of LC3B II and I levels revealed a significant increase in LCB3II/I ratio by LY294002. **e** Phagocytic activity in BV2 cells was assessed using pHrodo bioparticles and fluorescence emission was measured in the InCuCyte live cell imaging device in every 15 min. BV2 cells were treated with four different concentrations of PI3K inhibitor LY294002 (5  $\mu$ M – 50  $\mu$ M) and with 5  $\mu$ M Cytochalasin D (CytD). LY294002 decreased phagocytic activity dose-dependently ( $p < 0.001$ ) and CytD blocked phagocytosis almost completely. a-d; Data are presented as mean + SEM from four biological replicates. Mann-Whitney U-test, \* $p < 0.05$ , \*\* $p < 0.01$ , \*\*\* $p < 0.001$  vs. untreated control, # $p < 0.05$ , ## $p < 0.01$ , ### $p < 0.001$  vs. LPS control. **f** Phagocytic activity of primary microglia isolated from WT and Akt2 KO mice was assessed similarly as in BV2 cells using pHrodo bioparticles and fluorescence emission was measured in the InCuCyte live cell imaging device in every 30 min. Cells were treated with three different concentrations of LY294002 (1  $\mu$ M – 25  $\mu$ M) and with 5  $\mu$ M CytD. LY294002 decreased phagocytic activity dose-dependently ( $p < 0.001$ ) and Akt2 KO cells showed significantly decreased phagocytic activity as compared to WT cells ( $p < 0.001$ ). CytD blocked phagocytosis almost completely in both WT and Akt2 KO cells. e-f; Data are presented as mean + SEM from three biological replicates in technical quadruplets, One-way ANOVA, LSD (**e**) and Two-way ANOVA (**f**). **g** Levels of inflammatory markers, nitric oxide (NO), tumor necrosis factor  $\alpha$  (Tnfa), and interleukin 6 (Il6) were significantly lower in Akt2 KO primary microglia as compared to WT primary microglia after 48 h LPS + IFN $\gamma$  -treatment. Data presented as mean % + SEM,  $n = 3-4$ . \* $p < 0.05$ , \*\* $p < 0.01$ , T-test

to the recruitment of Syk kinase to activate downstream signaling molecules, such as PI3K, Erk, and phospholipase C $\gamma$ 2 (Plc $\gamma$ 2) [74]. To assess whether inhibition of PI3K exerts a similar effects also in microglia, the phosphorylation of Dap12 and Syk kinase (Y525/526, pSyk) by Src-kinase was stimulated by using macrophage colony stimulating factor (M-CSF) in mouse BV2 microglia with or without LY294002 (Fig. 6a-c). M-CSF is known to activate Dap12 and Syk kinase through outside-in signaling within minutes after the treatment [74, 75]. The treatment of BV2 cells with M-CSF for 5 min resulted in the expected ~ two-fold increase in pSyk levels ( $p < 0.001$ ) as compared to control cells, which was abolished by Src-kinase inhibitor SU665 as shown previously [75] (Fig. 6a and c). Unexpectedly, the combined treatment with LY294002 and M-CSF significantly increased the levels of pSyk in BV2 cells ( $p < 0.05$ , Fig. 6a-c). To further pinpoint the observed inhibitory effect of PI3K on pSyk levels in the Trem2/Dap12 signaling pathway, we used Trem2 antibody for direct ligand-induced activation of Trem2 alone or in combination with LY294002 for 5 min (Fig. 6d). Alpha-LISA-based analysis of pSyk showed an average 2.5-fold increase in the levels of pSyk after the treatment of primary microglia cultures with Trem2 antibody as compared to control cultures (Fig. 6d). Similar to the combined treatment with LY294002 and M-CSF in the BV2 cells, co-treatment of primary microglia with LY294002 and Trem2 antibody significantly further potentiated the increased levels of pSyk. These results suggest that the inhibition of PI3K activity increases Syk kinase activity upon ligand-induced activation of Trem2/Dap12 signaling in the microglia.

## Discussion

Typical western diet (TWD), which is manifested as increased intake of energy-dense foods high in saturated fat, sugar and cholesterol, and low in fiber, is a major contributor to the increasing prevalence of obesity and

T2D, imposing a global health challenge. Several studies have shown that TWD, obesity, and T2D increase the risk of AD [4, 6–10]. Despite these seminal studies, the underlying molecular mechanisms remain elusive. In human studies related to T2D and AD, the vascular contribution to the cognitive impairment and dementia is unequivocal [76], whereas the vascular contribution to the  $\beta$ -amyloid plaque or neurofibrillary pathology has been debated [76]. Human studies have also indicated that the breakdown of blood-brain barrier (BBB) contributes to cognitive dysfunction and the development of dementia in general (reviewed by Sweeney et al. [77]). Recently, it was suggested that damage in BBB and the degeneration of pericytes play a role in *APOE4*-associated cognitive decline independently of  $\beta$ -amyloid and Tau pathologies [78]. Transgenic mice provide an opportunity to assess the mechanistic links between T2D and AD without the confounding effects of atherosclerosis and the related hypoperfusion as the mice are highly resistant to atherosclerosis, even when exposed to TWD [79]. Furthermore, a recent study in APP<sup>swe</sup>/PS1<sup>dE9</sup> transgenic mice demonstrated that HFD exacerbates AD pathology in the brain, but does not impair the cerebral blood flow [80]. Here, we have assessed the effects of six-month TWD exposure on memory, brain pathology, and global gene expression in female mice with different genetic backgrounds linked to AD and/or tauopathy (A+ Tw, AwT+ and A+T+). In addition, we set the goal to address the translation of the mouse model-derived results to humans by utilizing cortical biopsies obtained from living iNPH patients presenting with  $\beta$ -amyloid pathology. In this unique human tissue sample set [81], we were able to specifically address T2D- and obesity-related effects in the frontal cortex of normal weight and obese iNPH patients with or without T2D. To our knowledge, this is the first study, which comprehensively addresses the full spectrum of AD-associated pathologies in parallel in several transgenic mouse lines and human



cortical tissue samples with  $\beta$ -amyloid pathology to elucidate TWD-, T2D, and obesity-related alterations in cellular processes.

We successfully induced obesity and diabetic phenotype in all of the mouse lines used by applying a six-month TWD regime, starting at the age of 7 months, which is in line with previous reports [13, 16, 20, 82]. Furthermore, TWD strongly increased fatty liver changes, emphasizing the robust effect of TWD on the metabolism not only in the brain but also in peripheral tissues, as also shown previously [83]. Our results related to the behavioral assessments strongly suggest that TWD-induced obesity and diabetic phenotype impair memory and learning, which are also supported by the previous findings [12–15, 18, 84, 85]. More specifically,

the comparison of the four genotypes suggests that adverse effects of TWD on memory and learning are the most prominent in mice with a moderate genetic predisposition to develop AD-like brain pathology (A+Tw and AwT+), while in the A+T+ mice, the strong genetic burden overpowers the effect of TWD. Previous studies have shown that TWD and HFD associate with increased risk of developing AD [86, 87], and cause more severe AD-associated neuropathological changes in various mouse models [88, 89]. Here, we observed a significantly increased number of phospho-Tau (AT8)-positive dystrophic neurites around  $\beta$ -amyloid plaques in both lateral entorhinal cortex and hippocampus in mice with A+Tw and A+T+ genotypes upon TWD. Although the assessment of dystrophic neurites in HC using 22C11

antibody did not completely corroborate the result obtained with AT8, TWD was found to significantly increase the 22C11-positive area around the  $\beta$ -amyloid plaques particularly in A + Tw mice. This is consistent with the result obtained with AT8 and in line with studies reporting comparable results with AT8 and 22C11 antibodies recognizing different epitopes and proteins (phosphorylated Tau and APP N-terminus, respectively) [66].

Some studies have reported that HFD or TWD does not have an effect on dystrophic neurites nor Tau pathology in APP<sup>swe</sup>/PS1<sup>dE9</sup> or Tau P301L mice, respectively [19, 90]. However, in an opposite experimental setup, Buccarello et al. showed fewer AT8-positive cells in the cortex and hippocampus of Tau P301L mice fed with low-fat and low-protein diet as compared to STD [91], suggesting that diet can modulate the dystrophic neurite pathology. In the present study, TWD or T+ genotype did not affect  $\beta$ -amyloid pathology in the lateral entorhinal cortex or hippocampus of mice with A+ genotype. This was not surprising, since we have shown previously that  $\beta$ -amyloid burden does not correlate with memory impairment in APP<sup>swe</sup>/PS1<sup>dE9</sup> mice [92]. Furthermore, several studies have reported adverse effects of HFD on memory and learning without exacerbating  $\beta$ -amyloid pathology in AD mouse models [14, 16, 93]. Conversely, other studies have suggested that HFD increases cortical  $\beta$ -amyloid load in APP<sup>swe</sup>/PS1<sup>dE9</sup> [94] and 3xTgAD mice [20]. To our knowledge, our study is the first that demonstrates an increased number of phospho-Tau (AT8)-positive dystrophic neurites around  $\beta$ -amyloid plaques in AD mouse models upon TWD. This is an important finding since dystrophic neurites are a hallmark of dense-core neuritic plaques, which are used in the neuropathological diagnosis of AD owing to their association with cognitive impairment [95].

Studies investigating diet-associated molecular mechanisms in APP23 transgenic mice have shown that HFD increases the expression of genes associated with immune response and inflammation, such as *Trem2*, *Tyrobp*, *P2ry12*, *Dock2* as well as a number of cytokines, chemokines and toll-like receptors [89]. Here, we observed a significant increase in the expression of *Trem2* and *Tyrobp* and other well-established DAM signature genes [32] as well as an enhanced transcriptional response for immune response-associated genes, suggesting an increased immune response in A+Tw and A+T+ mice upon TWD. It should be emphasized that A+Tw and A+T+ mice upon STD or TWD did not differ in their DAM response, highlighting the importance of  $\beta$ -amyloid as a driver for DAM response. However, further co-expression analyses of the transcriptomic alterations revealed that TWD, in fact, may have a suppressive impact on specific immune response genes in mice with

A+Tw or A+T+ genotypes. Detailed examination of the co-expression analysis of the identified subsets of genes indicated that the genes affected by TWD correlated with *Trem2* expression and were also intimately associated with the DAM signature [32]. This suggests that despite the enhanced expression of a subsets of genes, which associate with immune response, TWD suppresses the microglial response to  $\beta$ -amyloid pathology and that this repressive response is linked to *Trem2*-related processes, such as DAM activation. This molecular reprogramming of microglia upon TWD was further supported by the decreased Iba1 and Cd68 positivity around the  $\beta$ -amyloid plaques in TWD mice. These microglia showed no differences in the branching or process length with respect to genotype or diet, suggesting that morphological alterations cannot explain the decreased Iba1 positivity around  $\beta$ -amyloid plaques. Thus, both expressional and IHC analyses independently support the idea of a repressed immune response to TWD, which is eventually manifested as decreased number of microglia and increased number of dystrophic neurites around the  $\beta$ -amyloid plaques. Moreover, the decreased intensity of the lysosomal Cd68 may suggest that the functional capacity of the remaining microglia around the  $\beta$ -amyloid plaques is compromised.

Evaluation of the effects of TWD irrespective of the genotype also revealed a substantial overlap with altered expression of the previously described DAM genes. *Pik3r1*, encoding for p85 $\alpha$ , was one of the top hits in the DE analysis. Since *Pik3r1* was downregulated in the hippocampus by TWD irrespective of the genotype, we asked whether any key PI3K-Akt signaling pathway components were affected by TWD. Indeed, a decreased phosphorylation of Akt1/2 at the S473/S474 and T305/308/308 activation sites as well as at the inhibitory S9 site of Gsk3 $\beta$  were observed in the hippocampus of TWD mice. Our findings are in line with previous studies showing that the PI3K-Akt-Gsk3 $\beta$  signaling pathway is impaired in mouse and rat brain upon HFD and TWD [16, 84]. Interestingly, previous analyses in human post-mortem samples have demonstrated decreased levels of p85 $\alpha$  in the brain of AD patients [96] as well as in AD patients with co-morbid T2D [97]. Importantly, Liu et al. showed that the decrease in the levels of phosphorylated and total p85 $\alpha$  was more prominent in the brain of these comorbid patients as compared to AD patients without T2D, and that the alterations in p85 $\alpha$  coincided with altered phosphorylation of the downstream targets AKT and GSK3 $\beta$  [97]. Also, previous studies in different mouse models with a diabetic or obese phenotype have detected decreased levels of p85 $\alpha$  in the brain tissue [98]. Conversely, caloric restriction in Tg2576 mice led to increased protein levels of p85 $\alpha$  in the cerebral cortex as compared to control mice alongside with increased



activity of Akt1 [99]. In general, GSK3 $\beta$  is one of the main kinases phosphorylating Tau in the brain [25]. Thus, decreased phosphorylation of the inhibitory S9 site in Gsk3 $\beta$  upon TWD may explain the increased number of AT8-positive dystrophic neurites observed in our study. Supporting this idea, increased phosphorylation of Tau due to HFD or TWD in mice and rats has been observed also previously [16, 84, 100]. On the other hand, our biochemical analysis did not reveal clear changes in the levels of phosphorylated or total Tau by the TWD, which might be due to limited solubility of aggregated Tau protein with the extraction method used. In fact, there are also other studies, in which the effects of HFD or TWD on the phosphorylation status of Tau has not been conclusive in the biochemical assessments [14, 15, 20, 93].

Alterations of PI3K-Akt signaling are known to affect multiple cellular functions, such as autophagy, metabolism, proliferation, cell survival, and growth [101]. Here, we found increased levels of the autophagy markers p62 and LC3BI in the hippocampal total protein lysates of TWD mice, suggesting decreased autophagosomal activity. Given the decreased activation of Akt-kinase due to TWD, this was an unexpected finding since the activated Akt-kinase is known to activate mTORC1, which again inhibits the induction of autophagy [102]. However, our observation related to the increased p62 levels is consistent with previous studies reporting increased p62 levels in the peripheral tissues, hypothalamus, and hippocampus of mice on HFD [103–105]. Furthermore, HFD has been linked to impaired lysosomal activity [105]. These findings suggest that also other pathways in addition to PI3K-Akt signaling pathway control autophagy. Indeed, 5' AMP-activated protein kinase (AMPK) is a conserved sensor of nutritional status, which may affect autophagy independently of mTORC1 [106]. Since starvation is a well-known inducer of autophagy, the opposite condition with high energy supply, such as TWD, may result in reduced autophagy.

The fact that *Pik3r1* is abundantly expressed in mouse microglia [62] together with our RNA-sequencing data prompted us to elucidate mouse microglial functions upon downregulation of PI3K-Akt signaling by both pharmacological and genetic approaches. Inhibition of PI3K-Akt signaling using LY294002 both in mouse BV2 and primary microglia significantly decreased the phagocytic uptake of bioparticles in a dose-dependent manner. A similar decrease was observed in the primary microglia isolated from Akt2 KO mice. Interestingly, the treatment of Akt2 KO microglia with LY294002 further reduced the phagocytic uptake of bioparticles, suggesting that PI3K-Akt pathway as a whole entity plays a key role in the regulation of phagocytic activity in microglia. LPS treatment of Akt2 KO microglia cultures reduced the levels of the inflammatory mediators Tnf- $\alpha$ , Il6 and NO

in the culture medium, which agrees with the previous findings indicating that Akt2 KO macrophages are hyporesponsive to LPS [107]. Apart from being the regulatory subunit of PI3K, p85 $\alpha$  encompasses a significant role in controlling the actin organization and cell migration, independently of PI3K activity [108]. Therefore, it is possible that the reduction in the expression of *Pik3r1* owing to TWD does not only affect PI3K activity, but also other functions that are relevant for microglia. On the other hand, studies in *Pik3r1* knock-out mice have revealed that the lack of p85 $\alpha$  subunit reduced the activity of PI3K and Akt in the peritoneal exudate cells upon LPS-induced stress [109]. Moreover, the LPS treatment of *Pik3r1* knock-out mouse cells induced the expression of *Tnf* and *Il6* as well as increased the nuclear localization of phosphorylated transcription factor ATF-2, known to increase proinflammatory cytokine expression in LPS-stimulated monocytes [109]. In conclusion, modulation of the activity of PI3K-Akt signaling pathway affects central functions of microglia, such as phagocytic uptake, autophagosomal degradation, and proinflammatory response against different stressors, including  $\beta$ -amyloid. In this context, TWD-associated reduction in the expression of *Pik3r1* encoding p85 $\alpha$  may significantly contribute to the observed suppressive immune response and reduced clustering of microglia around the  $\beta$ -amyloid plaques. On the other hand, the results from the IHC analysis of p85 $\alpha$  were partially conflicting, since the area and intensity of p85 $\alpha$  around  $\beta$ -amyloid plaques was increased upon TWD in A + Tw mice, while in A + T+ mice, the effect was the opposite. However, this type of genotype dependency is also observed in the RNA-sequencing data, where the most aberrant effects on transcriptional response were observed in A + T+ mice.

Several studies have reported that HFD affects particularly microglial phenotype, function and/or inflammatory outcomes [90, 110, 111]. Trem2 has been shown to play a central role in AD and one of its functions is to act as a lipid-sensing receptor affecting microglial response [59]. In addition to microglia and cells of myeloid origin (e.g. monocytes, macrophages and osteoclasts), Trem2 is also expressed in mature adipocytes [112], and has been shown to affect insulin resistance in HFD mice through adipose tissue remodeling [113]. These reports emphasize that alterations in Trem2 signaling may also mediate the effects of HFD or TWD. Related to this, we now show that the ligand-induced activation of Trem2/Dap12 both directly (Trem2 antibody) and indirectly (M-CSF) upon the inhibition of PI3K-Akt signaling enhanced the activation of Syk kinase in mouse microglia. This was an unexpected result since it has been previously shown that the inhibition of PI3K in macrophages and osteoclasts prevented the recruitment of p85 $\alpha$  and Syk kinase to Dap12, leading to reduced downstream signaling via other mediators, such as

Plcy2 [74]. Whether the observed increase in Syk kinase activation is a compensatory effect for the reduced downstream signaling in microglia remains to be determined in future studies. Collectively, these results highlight the seminal role of p85 $\alpha$ /PI3K in the activation of Trem2/Dap12 signaling pathway, particularly in the formation and activation of Syk kinase complex in microglia. Recent studies suggest that impaired Trem2-Akt-mTOR signaling in AD patients carrying *TREM2* risk variants and in Trem2-deficient mice with AD-like microglia affects autophagy and metabolism [34] and decreases the ability of microglia to form a protective barrier around  $\beta$ -amyloid plaques, leading to axonal dystrophy [114]. The findings of the present study, including the increased number of dystrophic neurites and impaired PI3K-Akt signaling, large range of transcriptional changes in the microglial genes due to TWD and/or A+ genotype, and decreased Iba1 and Cd68 immunoreactivity around  $\beta$ -amyloid plaques similarly to previous studies, suggest that indeed impaired PI3K-Akt signaling reduces microglia clustering and their ability to form a protective barrier around plaques [34, 114]. Consequently, this may lead to leakage of toxic  $\beta$ -amyloid aggregates disturbing neuronal integrity. Our observation that TWD increased the number of AT8-positive dystrophic neurites around the  $\beta$ -amyloid plaques supports this hypothesis. RNA-sequencing did not reveal major alterations in the expression of *Gfap*, suggesting that TWD does not affect astrocyte reactivity. Interestingly, some mouse studies suggest that at least part of the detrimental effects of HFD or TWD are reversible when the diet is changed to standard or low-fat diet [115–117]. However, we speculate that the potential reversibility depends on the age of mice when the diet change takes place and also on the duration of diet treatment, so that the older HFD or TWD mice may show slower recovery or no recovery at all. It is also tempting to speculate that the activation of Trem2 signaling in microglia using e.g. monoclonal antibodies developed against the Trem2 receptor [118, 119] could actually mitigate the impaired downstream signaling of Trem2 and PI3K-Akt in mice upon TWD. This is a conceivable prospect given that certain monoclonal Trem2 antibodies show a dual mechanism of action by stabilizing Trem2 on the cell surface and reducing its shedding, and concomitantly activating the downstream p-Syk signaling [118].

In order to elucidate whether similar alterations to those observed in microglia in the TWD mice could also be detected in human brain tissue, we utilized frontal cortical brain biopsies obtained from iNPH patients harboring  $\beta$ -amyloid pathology. Brain biopsies taken during shunt surgery offer a unique window into the brain tissue of living iNPH patients to examine the early stages of AD-related brain pathology [81]. We found that the combination of obesity and T2D led to presence of fewer microglia

around the  $\beta$ -amyloid plaques compared to normal weight and obese iNPH patients without T2D, which is well in concordance with our findings in mice with the TWD-induced diabetic phenotype. Neuropathological examination revealed no Tau pathology (AT8 immunoreactivity) in the cortical tissue samples from the iNPH patients with respect to normal weight, obese, or diabetic phenotype, suggesting that  $\beta$ -amyloid drives the microglial alterations in the brain of these patients. Altered microglial response to  $\beta$ -amyloid plaques due to T2D has been suggested earlier, although no quantitative data have been presented [120]. Interestingly, increased microglial dystrophy has been reported in the hypothalamus of obese individuals [110] as well as in the hippocampus and several cortical areas in AD patients [121, 122].

## Conclusions

Collectively, our results together with previous studies in both mouse and human support the idea that obesity and T2D contribute to microglial dysfunction. According to our present data, particularly T2D-related metabolic changes appear to disturb microglial function around  $\beta$ -amyloid plaques. We have focused here on the most prominent effects of TWD in mice with different AD- and/or tauopathy-associated genetic backgrounds. However, the identified novel targets and regulatory networks associated with the individual genotypes (AwT+, A+Tw, and A+T+) will set the basis for further elucidation of the underlying mechanisms related to the comorbidity of AD and T2D. Moreover, the fact that similar results were obtained in the brain tissue of TWD mice and iNPH patients with T2D lays an outstanding foundation to test novel therapeutic interventions, focusing specifically on the microglial response and clustering against AD-associated pathologies in the brain.

## Supplementary Information

The online version contains supplementary material available at <https://doi.org/10.1186/s13024-020-00415-2>.

**Additional file 1: Supplementary Figure S1.** a-c. Assessment of soluble A $\beta$ 42 and A $\beta$ 40 levels as well as A $\beta$ 42 and A $\beta$ 40 ratio of hippocampal samples from mice with A+ transgene (APP<sup>swe</sup>/PS1<sup>dE9</sup>) revealed no significant diet effect. Data are presented as mean  $\pm$  SEM,  $n = 5-6$ , Two-way ANOVA. d Representative immunofluorescence images of  $\beta$ -amyloid plaques stained with X-34 (blue) surrounded by 22C11-positive dystrophic neurites (red), and Iba1-positive microglia (green) from A+Tw and A+T+ mice from both STD and TWD groups. Scale bar 10  $\mu$ m. e Counting of 22C11-positive neurites revealed no diet nor genotype effect. f Quantification of 22C11-positive area (pixels) around  $\beta$ -amyloid plaques revealed a statistically significant genotype  $\times$  diet interaction ( $p < 0.001$ ). TWD significantly increased the 22C11-positive area ( $p = 0.001$ ), while T+ transgene (Tau P301L) had an opposing effect on the 22C11-positive area depending on the diet. d-f; results are shown as mean  $\pm$  SEM,  $n = 5-6$  mice/group, Two-Way ANOVA. g A representative Western blot image of hippocampal lysates and quantification phospho-Tau and total Tau levels. Phosphorylated protein levels were normalized to their respective total protein levels in cell lysates and total protein levels were normalized to

$\beta$ -actin. All results are shown as mean + SEM,  $n = 5-7$  mice/group, Two-way ANOVA. A+Tw = APPswe/PS1dE9, A+T+ = APPswe/PS1dE9 x Tau P301L. **Supplementary Figure S2.** a. Heatmap of z-score values for transcripts specifically mapping to human (h) *APP*, *PSEN1*, and *MAPT*, show a significant increase in *APP* and *PSEN1* in A+Tw and A+T+ mice, and a significant increase in *MAPT* levels for AwT+ and A+T+ mice as compared to AwTw mice. b PCA for all samples (AwTw, AwT+, A+Tw, A+T+ STD/TWD). c PCA for samples of each genotype showing segregation due to TWD. d Number of DE genes (FDR < 0.05) for each genotype/diet combination as compared to corresponding diet AwTw mice. e Venn diagram showing overlap of DE genes between genotype/diet groups.  $n = 4-6$  mice/group. AwTw = wild-type, AwT+ = Tau P301L, A+Tw = APPswe/PS1dE9, A+T+ = APPswe/PS1dE9 x Tau P301L. **Supplementary Figure S3.** a. Heatmap of z-score values for genes with  $Z > 2.5$  or  $< -2.5$  in Fig. 2a for STD mice, but not TWD mice for either A+Tw vs AwTw mice (left) or A+T+ vs AwTw mice (right). b Dotplots representing enrichment scores (color = FDR, size = gene ratio) for pathways associated with significantly down- and upregulated genes in TWD AwTw mice as compared to STD AwTw mice (left plot) and for genes, which show  $Z > 2.5$  or  $< -2.5$  in Fig. 2a in TWD mice, but not STD mice for genetic backgrounds AwT+, A+Tw, and A+T+ (right plot). c Correlating and hierarchical clustering of modules in STD or TWD networks. d Cell type enrichment of genes in network modules. e Box plots representing eigengene values for modules negatively associated with genotype. Points represent eigengene values for each mouse in that group. Box plots show the median, 25th and 75th percentiles, error bars show 1.5 interquartile ranges.  $n = 4-6$  mice/group. AwTw = wild-type, AwT+ = Tau P301L, A+Tw = APPswe/PS1dE9, A+T+ = APPswe/PS1dE9 x Tau P301L. **Supplementary Figure S4.** Expression profiles of Trem2, Pi3k-Akt, and Wnt signaling pathways. a Left heatmap: Gene expression levels (as z-score values) for genes enriched in Fig. 2d regarding terms "Genes correlated ( $r > 0.5$ ) with Trem2", "Genes correlated ( $r > 0.3$ ) with Trem2", "Upregulated in AD-associated microglia (Keren-Shaul)", and "Regulation of canonical Wnt signaling pathway". Right heatmap: respective log<sub>2</sub> fold change (log<sub>2</sub>(FC)) values from TWD vs. STD comparison. Highlighted are top significantly up- and down-regulated genes for TWD vs. STD comparison regarding each term (FDR < 0.05, max. 15 up- or down-regulated genes). b Left heatmap: gene expression levels (as z-score values) for differentially expressed genes in TWD vs. STD comparison (FDR < 0.05) associated with pathways related to Trem2- (<https://www.wikipathways.org/index.php/Pathway:WP3626>), Pi3k-Akt- (<https://www.wikipathways.org/index.php/Pathway:WP2841>), or Wnt (<https://www.wikipathways.org/index.php/Pathway:WP403>). Right heatmap: respective log<sub>2</sub> fold change (log<sub>2</sub>(FC)) values from TWD vs. STD comparison. On the right side of the heatmaps are indicated the genes associated with the corresponding pathways. **Supplementary Figure S5.** a. *Pik3r1*, *Trem2*, and *Tyrbp* expression levels obtained from RNA-sequencing, and b from qPCR. c Assessment of microglia morphology around  $\beta$ -amyloid plaques by quantification of the number of process endpoints/cell (left) or process length/cell ( $\mu$ m, right). Data are presented as mean + SEM,  $n = 20$  A+Tw STD,  $n = 43$  A+Tw TWD,  $n = 11$  A+T+ STD,  $n = 28$  A+T+ TWD, Two-way ANOVA. d Heatmap of z-score values for selected microglia-specific markers in different genotype and diet groups. AwTw = wild-type, AwT+ = Tau P301L, A+Tw = APPswe/PS1dE9, A+T+ = APPswe/PS1dE9 x Tau P301L. **Supplementary Figure S6.** a. Quantification of Western blot shown in Fig. 5 revealed that 10  $\mu$ M LY294002 together with LPS increased LC3B II levels as compared to both untreated and LPS-treated controls ( $p < 0.05$ , One-way ANOVA, LSD posthoc). b LY294002 treatment with or without LPS had no effect on LC3B I levels (Welch's ANOVA, Tamhane's posthoc). c Quantification revealed increased total Akt level in samples treated together with LPS and 1  $\mu$ M LY294002 as compared to untreated samples (UNT,  $p < 0.05$ , Welch's ANOVA, Tamhane's posthoc) d Quantification of p85a levels showed significantly decreased levels in samples treated together with LPS and 10  $\mu$ M LY294002 as compared to both UNT and LPS treated control samples ( $p < 0.05$ , Welch's ANOVA, Tamhane's posthoc). e A representative Western blot image from lysates of BV2 cells treated with LY294002 (LY) (0.1  $\mu$ M - 10  $\mu$ M), and f with LY294002 together with LPS. g Quantification revealed decreased phosphorylation status of Erk1 and 2 (pErk1 and 2) in Y204 site in a dose-dependent manner in samples treated with LY294002 or treated together with LPS and LY294002 (One-way ANOVA, LSD posthoc).

h Quantification of total Erk2 levels showed an increase in cells treated with 0.1  $\mu$ M and 1  $\mu$ M LY294002 together with LPS (One-way ANOVA, LSD posthoc). i and j Quantification revealed no changes in pro-caspase-3 or in active caspase-3 levels (Welch's ANOVA). Phosphorylated protein levels were normalized to their respective total protein levels in cell lysates and total protein levels were normalized to  $\beta$ -actin. Data are presented as mean + SEM from four biological replicates. \* $p < 0.05$ , \*\* $p < 0.01$ , \*\*\* $p < 0.001$  vs. untreated control, # $p < 0.05$ , ## $p < 0.01$ , ### $p < 0.001$  vs. LPS control.

**Additional file 2: Supplementary Table S1.** Differential expression analysis results for AwT+, A+Tw, and A+T+ vs AwTw, STD mice.

**Additional file 3: Supplementary Table S2.** Differential expression analysis results for AwT+, A+Tw, and A+T+ vs AwTw, TWD mice.

**Additional file 4: Supplementary Table S3.** Enrichment analysis for differentially expressed genes in AwT+, A+Tw, and A+T+ vs AwTw comparison for both STD and TWD mice.

**Additional file 5: Supplementary Table S4.** Enrichment analysis for genes showing discordant response to  $\beta$ -amyloid- and/or Tau-pathology upon TWD (Fig. 2a, blue dot genes).

**Additional file 6: Supplementary Table S5.** WGCNA module assignment and membership values.

**Additional file 7: Supplementary Table S6.** Enrichment analysis for WGCNA module genes.

**Additional file 8: Supplementary Table S7.** Differential expression analysis results for TWD vs STD mice.

**Additional file 9: Supplementary Table S8.** Enrichment analysis for differentially expressed genes upon TWD.

## Abbreviations

AD: Alzheimer's disease; Akt (PKB): Protein kinase B; APPswe: Amyloid precursor protein 695 harboring the Swedish K670M/N671L mutations; DAM: Disease-associated microglia; GSK3 $\beta$ : Glycogen synthase kinase; GTT: Glucose tolerance test; HC: Hippocampus; HFD: High fat diet; IBA1: Ionized calcium-binding adapter molecule 1; iNPH: Idiopathic normal pressure hydrocephalus; LC3B: Microtubule-associated proteins 1A/1B light chain 3B; LEC: Lateral entorhinal cortex; LPS: Lipopolysaccharide; MAPK: The Ras-mitogen-activated protein kinase; M-CSF: Macrophage-Colony Stimulating Factor; mTORC1: Mammalian target of Rapamycin complex 1; PI3K: Phosphoinositide 3-kinase; PS1dE9: Presenilin 1 with the exon-9 deletion; SYK: Spleen tyrosine kinase; STD: Standard diet; TREM2: Triggering receptor expressed on myeloid cells 2; TNF $\alpha$ : Tumor necrosis factor  $\alpha$ ; T2D: Type 2 diabetes; TWD: Typical Western diet

## Acknowledgements

We thank Finnish Functional Genomics Centre supported by University of Turku, Åbo Akademi University and Biocenter Finland. Part of the work was carried out with the support of UEF Cell and Tissue Imaging Unit, University of Eastern Finland, Finland. The computational analyses were performed on servers provided by UEF Bioinformatics Center, University of Eastern Finland, Finland.

## Authors' contributions

TN, HM, SG, SK, MT, LL, SR and PM performed all biochemical analyses and in vitro experiments. HK, HS, and PMi performed animal experiments. HM, SKa, ER, SJ, and PMi performed immunohistochemical analyses. MM and TK performed bioinformatics analyses. BK, TR, JP, and VL provided and characterized human tissue material. TN, HM, and HT analyzed the data, and performed statistical analyses. TN, HM, MM, AH, HT and MH wrote the manuscript. HT and MH conceived of the study, research design, obtained study funding, and supervised all aspects of the study. All authors critically read and approved the final manuscript.

## Funding

This study was supported by grants from Academy of Finland (grant numbers 288659, 307866, 315459), Sigrid Jusélius Foundation, The Strategic Neuroscience Funding of the University of Eastern Finland, JPCo-fuND2 Personalised Medicine for Neurodegenerative Diseases (grant number 334802), Doctoral Programme in Molecular Medicine (DPM) at the University of

Eastern Finland, and European Union Horizon 2020 research and innovation programme (grant number 692340).

#### Availability of data and materials

Results generated and analyzed during the current study are included in this published article and its supplementary files. The RNA-seq data has been deposited to the GEO database (<https://www.ncbi.nlm.nih.gov/geo/>) under accession number GSE144746.

#### Ethics approval and consent to participate

All animal procedures were carried out in accordance with the guidelines of the European Community Council Directives 86/609/EEC and approved by the Animal Experiment Board of Finland. All patients gave their written informed consent, prior to the surgery, for the study accepted by Ethics Committee, Hospital District of Northern Savo.

#### Consent for publication

Not applicable.

#### Competing interests

The authors declared no potential conflicts of interest with respect to the research, authorship, and/or publication of this article.

#### Author details

<sup>1</sup>Institute of Biomedicine, University of Eastern Finland, P.O. Box 1627, FI-70211 Kuopio, Finland. <sup>2</sup>A. I. Virtanen Institute for Molecular Sciences, University of Eastern Finland, Kuopio, Finland. <sup>3</sup>Department of Simulation and Virtual Medical Education, Faculty of Medicine, Comenius University, Bratislava, Slovak Republic. <sup>4</sup>Department of Neurosurgery, Kuopio University Hospital, and Institute of Clinical Medicine, Unit of Neurosurgery, University of Eastern Finland, Kuopio, Finland. <sup>5</sup>Department of Pathology, Kuopio University Hospital, and Institute of Clinical Medicine, Unit of Pathology, University of Eastern Finland, Kuopio, Finland. <sup>6</sup>Department of Clinical Nutrition, Institute of Public Health and Clinical Nutrition, University of Eastern Finland, Kuopio, Finland.

Received: 28 April 2020 Accepted: 26 October 2020

Published online: 10 November 2020

#### References

- Bloom GS. Amyloid- $\beta$  and tau: the trigger and bullet in Alzheimer disease pathogenesis. *JAMA Neurol.* 2014;71(4):505–8.
- Montine TJ, Phelps CH, Beach TG, Bigio EH, Cairns NJ, Dickson DW, et al. National institute on aging-Alzheimer's association guidelines for the neuropathologic assessment of Alzheimer's disease: a practical approach. *Acta Neuropathol.* 2012;123:1–11.
- Hong S, Beja-Glasser VF, Nfonoyim BM, Frouin A, Li S, Ramakrishnan S, et al. Complement and microglia mediate early synapse loss in Alzheimer mouse models. *Science* (80- ). 2016;352:712–6.
- Irie F, Fitzpatrick AL, Lopez OL, Kuller LH, Peila R, Newman AB, et al. Enhanced risk for Alzheimer disease in persons with type 2 diabetes and APOE epsilon4: the cardiovascular health study cognition study. *Arch Neurol.* 2008;65(1):89–93.
- De Felice FG, Ferreira ST. Inflammation, defective insulin signaling, and mitochondrial dysfunction as common molecular denominators connecting type 2 diabetes to Alzheimer disease. *Diabetes.* 2014;63(7):262–72.
- Eskelinen MH, Ngandu T, Helkala EL, Tuomilehto J, Nissinen A, Soininen H, et al. Fat intake at midlife and cognitive impairment later in life: a population-based CAIDE study. *Int J Geriatr Psychiatry.* 2008;23:741–7.
- Grant WB. Dietary links to Alzheimer's disease: 1999 update. *J Alzheimers Dis.* 1999;1(4-5):197–201.
- Kivipelto M, Ngandu T, Fratiglioni L, Viitanen M, Kåreholt I, Winblad B, et al. Obesity and vascular risk factors at midlife and the risk of dementia and Alzheimer disease. *Arch Neurol.* 2005;62:1556–60.
- Laitinen MH, Ngandu T, Rovio S, Helkala EL, Uusitalo U, Viitanen M, et al. Fat intake at midlife and risk of dementia and Alzheimer's disease: a population-based study. *Dement Geriatr Cogn Disord.* 2006;22:99–107.
- Xu WL, Von Strauss E, Qiu CX, Winblad B, Fratiglioni L. Uncontrolled diabetes increases the risk of Alzheimer's disease: a population-based cohort study. *Diabetologia.* 2009;52(6):1031–9.
- Winzell MS, Ahren B. The high-fat diet-fed mouse: a model for studying mechanisms and treatment of impaired glucose tolerance and type 2 diabetes. *Diabetes.* 2004;53(Suppl 3):S215–9.
- Hascup ER, Broderick SO, Russell MK, Fang Y, Bartke A, Boger HA, et al. Diet-induced insulin resistance elevates hippocampal glutamate as well as VGLUT1 and GFAP expression in A $\beta$ PP/PS1 mice. *J Neurochem.* 2019;148:219–37.
- Hiltunen M, Khandelwal VKM, Yaluri N, Tiilikainen T, Tusa M, Koivisto H, et al. Contribution of genetic and dietary insulin resistance to Alzheimer phenotype in APP/PS1 transgenic mice. *J Cell Mol Med.* 2012;16:1206–22.
- Knight EM, Martins IVA, Gümüşgöz S, Allan SM, Lawrence CB. High-fat diet-induced memory impairment in triple-transgenic Alzheimer's disease (3xTgAD) mice is independent of changes in amyloid and tau pathology. *Neurobiol Aging.* 2014;35:1821–32.
- Sah SK, Lee C, Jang JH, Park GH. Effect of high-fat diet on cognitive impairment in triple-transgenic mice model of Alzheimer's disease. *Biochem Biophys Res Commun.* 2017;493:731–6.
- Petrov D, Pedrós I, Artiach G, Sureda FX, Barroso E, Pallàs M, et al. High-fat diet-induced deregulation of hippocampal insulin signaling and mitochondrial homeostasis deficiencies contribute to Alzheimer disease pathology in rodents. *Biochim Biophys Acta - Mol Basis Dis.* 1852;2015:1687–99.
- Kothari V, Luo Y, Tornabene T, O'Neill AM, Greene MW, Geetha T, et al. High fat diet induces brain insulin resistance and cognitive impairment in mice. *Biochim Biophys Acta - Mol Basis Dis.* 1863;2017:499–508.
- Jeong JH, Koo JH, Cho JY, Kang EB. Neuroprotective effect of treadmill exercise against blunted brain insulin signaling, NADPH oxidase, and tau hyperphosphorylation in rats fed a high-fat diet. *Brain Res Bull.* 2018;142:374–83.
- Gratuzé M, Julien J, Morin F, Calon F, Hébert SS, Marette A, et al. High-fat, high-sugar, and high-cholesterol consumption does not impact tau pathogenesis in a mouse model of Alzheimer's disease-like tau pathology. *Neurobiol Aging.* 2016;47:71–3.
- Julien C, Tremblay C, Phivilay A, Berthiaume L, Émond V, Julien P, et al. High-fat diet aggravates amyloid-beta and tau pathologies in the 3xTg-AD mouse model. *Neurobiol Aging.* 2010;31:1516–31.
- Wakabayashi T, Yamaguchi K, Matsui K, Sano T, Kubota T, Hashimoto T, et al. Differential effects of diet- and genetically-induced brain insulin resistance on amyloid pathology in a mouse model of Alzheimer's disease. *Mol Neurodegener.* 2019;14:15.
- Chiu S-L, Chen C-M, Cline HT. Insulin receptor signaling regulates synapse number, dendritic plasticity, and circuit function in vivo. *Neuron NIH Public Access.* 2008;58:708–19.
- Zhao WQ, Townsend M. Insulin resistance and amyloidogenesis as common molecular foundation for type 2 diabetes and Alzheimer's disease. *Biochim Biophys Acta - Mol Basis Dis.* 2009;1792(5):482–96.
- Kim B, Feldman EL. Insulin resistance in the nervous system. *Trends Endocrinol Metab.* 2012;23(3):133–41.
- Iqbal K, Liu F, Gong CX. Tau and neurodegenerative disease: the story so far. *Nat Rev Neurol.* 2016;12(1):15–27.
- Son JH, Shim JH, Kim KH, Ha JY, Han JY. Neuronal autophagy and neurodegenerative diseases. *Exp Mol Med.* 2012;44(2):89–98.
- Heras-Sandoval D, Pérez-Rojas JM, Hernández-Damián J, Pedraza-Chaverri J. The role of PI3K/AKT/mTOR pathway in the modulation of autophagy and the clearance of protein aggregates in neurodegeneration. *Cell Signal.* 2014;26(12):2694–701.
- Swardfager W, Lanctt K, Rothenburg L, Wong A, Cappell J, Herrmann N. A meta-analysis of cytokines in Alzheimer's disease. *Biol Psychiatry.* 2010;68:930–41.
- Sjöholm Å, Nyström T. Inflammation and the etiology of type 2 diabetes. *Diabetes Metab Res Rev.* 2006;22(1):4–10.
- Sims R, Van Der Lee SJ, Naj AC, Bellenguez C, Badarinarayan N, Jakobsdottir J, et al. Rare coding variants in PLCG2, ABI3, and TREM2 implicate microglial-mediated innate immunity in Alzheimer's disease. *Nat Genet.* 2017;49:1373–84.
- Nott A, Holtman IR, Coufal NG, Schlachetzki JCM, Yu M, Hu R, et al. Brain cell type-specific enhancer-promoter interactome maps and disease-risk association. *Science* (80- ). 2019;366:1134–9.

32. Keren-Shaul H, Spinrad A, Weiner A, Matcovitch-Natan O, Dvir-Szternfeld R, Ulland TK, et al. A unique microglia type associated with restricting development of Alzheimer's disease. *Cell*. 2017;169:1276–1290.e17.
33. Krasemann S, Madore C, Cialic R, Baufeld C, Calcagno N, El Fatimy R, et al. The TREM2-APOE pathway drives the transcriptional phenotype of dysfunctional microglia in neurodegenerative diseases. *Immunity*. 2017;47:566–581.e9.
34. Ulland TK, Song WM, Huang SCC, Ulrich JD, Sergushichev A, Beatty WL, et al. TREM2 maintains microglial metabolic fitness in Alzheimer's disease. *Cell*. 2017;170:649–663.e13.
35. Jankowsky JL, Fadale DJ, Anderson J, Xu GM, Gonzales V, Jenkins NA, et al. Mutant presenilins specifically elevate the levels of the 42 residue  $\beta$ -amyloid peptide in vivo: evidence for augmentation of a 42-specific  $\gamma$  secretase. *Hum Mol Genet*. 2004;13(2):159–70.
36. Kimura T, Fukuda T, Sahara N, Yamashita S, Murayama M, Mizoroki T, et al. Aggregation of detergent-insoluble tau is involved in neuronal loss but not in synaptic loss. *J Biol Chem*. 2010;285:38692–9.
37. Gould TJ, Burke D, Bewersdorf J, Booth MJ. Adaptive optics enables 3D STED microscopy in aberrating specimens. *Opt Express*. 2012;20(19):20998–1009.
38. Schindelin J, Arganda-Carreras I, Frise E, Kaynig V, Longair M, Pietzsch T, et al. Fiji: an open-source platform for biological-image analysis. *Nat Methods*. 2012;9(7):676–82.
39. Relkin N, Marmarou A, Klinge P, Bergsneider M, Black PM. Diagnosing idiopathic normal-pressure hydrocephalus. *Neurosurgery*. 2005;57. <https://doi.org/10.1227/01.NEU.0000168185.29659.C5>.
40. Junkkari A, Luikku AJ, Danner N, Jyrkkänen HK, Rauramaa T, Korhonen VE, et al. The Kuopio idiopathic normal pressure hydrocephalus protocol: initial outcome of 175 patients. *Fluids Barriers CNS*. 2019;16:21.
41. Luikku AJ, Hall A, Nerg O, Koivisto AM, Hiltunen M, Helisalmi S, et al. Predicting development of Alzheimer's disease in patients with shunted idiopathic normal pressure hydrocephalus. *J Alzheimers Dis*. 2019;71:1233–43.
42. Gresa-Arribas N, Viéitez C, Dentesano G, Serratos J, Saura J, Solà C. Modelling neuroinflammation in vitro: a tool to test the potential neuroprotective effect of anti-inflammatory agents. *PLoS One*. 2012;7:e45227.
43. Natunen TA, Gynther M, Rostalski H, Jaako K, Jalkanen AJ. Extracellular prolyl oligopeptidase derived from activated microglia is a potential neuroprotection target. *Basic Clin Pharmacol Toxicol*. 2019;124:40–9.
44. Gabbouj S, Natunen T, Koivisto H, Jokivarsi K, Takalo M, Marttinen M, et al. Intranasal insulin activates Akt2 signaling pathway in the hippocampus of wild-type but not in APP/PS1 Alzheimer model mice. *Neurobiol Aging*. 2019;75:98–108.
45. Livak KJ, Schmittgen TD. Analysis of relative gene expression data using real-time quantitative PCR and the 2- $\Delta\Delta$ CT method. *Methods*. 2001;25:402–8.
46. Bolger AM, Lohse M, Usadel B. Trimmomatic: a flexible trimmer for Illumina sequence data. *Bioinformatics*. 2014;30:2114–20.
47. Langmead B, Salzberg SL. Fast gapped-read alignment with Bowtie 2. *Nat Methods*. 2012;9:357–9.
48. Bray NL, Pimentel H, Melsted P, Pachter L. Near-optimal probabilistic RNA-seq quantification. *Nat Biotechnol*. 2016;34:525–7.
49. Sonesson C, Love MI, Robinson MD. Differential analyses for RNA-seq: transcript-level estimates improve gene-level inferences [version 2; referees: 2 approved]. *F1000Res*. 2016;4:1521.
50. Love MI, Huber W, Anders S. Moderated estimation of fold change and dispersion for RNA-seq data with DESeq2. *Genome Biol*. 2014;15(12):550.
51. Ritchie ME, Phipson B, Wu D, Hu Y, Law CW, Shi W, et al. Limma powers differential expression analyses for RNA-sequencing and microarray studies. *Nucleic Acids Res*. 2015;43:e47.
52. Langfelder P, Horvath S. WGCNA: an R package for weighted correlation network analysis. *BMC Bioinformatics*. 2008;9:559.
53. Miller JA, Cai C, Langfelder P, Geschwind DH, Kurian SM, Salomon DR, et al. Strategies for aggregating gene expression data: the collapseRows R function. *BMC Bioinformatics*. 2011;12:322.
54. Subramanian A, Tamayo P, Mootha VK, Mukherjee S, Ebert BL, Gillette MA, et al. Gene set enrichment analysis: a knowledge-based approach for interpreting genome-wide expression profiles. *Proc Natl Acad Sci U S A*. 2005;102:15545–50.
55. Chen EY, Tan CM, Kou Y, Duan Q, Wang Z, Meirelles GV, et al. Enrichr: interactive and collaborative HTML5 gene list enrichment analysis tool. *BMC Bioinformatics*. 2013;14:128.
56. Butovsky O, Jedrychowski MP, Moore CS, Cialic R, Lanser AJ, Gabrieli G, et al. Identification of a unique TGF- $\beta$ -dependent molecular and functional signature in microglia. *Nat Neurosci*. 2014;17:131–43.
57. Galatro TF, Holtman IR, Lerario AM, Vainchtein ID, Brouwer N, Sola PR, et al. Transcriptomic analysis of purified human cortical microglia reveals age-associated changes. *Nat Neurosci*. 2017;20:1162–71.
58. Gokce O, Stanley GM, Treutlein B, Neff NF, Camp JG, Malenka RC, et al. Cellular taxonomy of the mouse striatum as revealed by single-cell RNA-Seq. *Cell Rep*. 2016;16:1126–37.
59. Wang Y, Cella M, Mallinson K, Ulrich JD, Young KL, Robinette ML, et al. TREM2 lipid sensing sustains the microglial response in an Alzheimer's disease model. *Cell*. 2015;160:1061–71.
60. Aibar S, González-Blas CB, Moerman T, Huynh-Thu VA, Imrichova H, Hulselmans G, et al. SCENIC: single-cell regulatory network inference and clustering. *Nat Methods*. 2017;14:1083–6.
61. Seyfried NT, Dammer EB, Swarup V, Nandakumar D, Duong DM, Yin L, et al. A multi-network approach identifies protein-specific co-expression in asymptomatic and symptomatic Alzheimer's disease. *Cell Syst*. 2017;4:60–72.e4.
62. Zhang Y, Chen K, Sloan SA, Bennett ML, Scholze AR, O'Keefe S, et al. An RNA-sequencing Transcriptome and splicing database of glia, neurons, and vascular cells of the cerebral cortex. *J Neurosci*. 2014;34:11929–47 Available from: <http://www.jneurosci.org/cgi/doi/10.1523/JNEUROSCI.1860-14.2014>.
63. Rodgers SP, Born HA, Das P, Jankowsky JL. Transgenic APP expression during postnatal development causes persistent locomotor hyperactivity in the adult. *Mol Neurodegener*. 2012;7:28.
64. Kempainen S, Rantamäki T, Jerónimo-Santos A, Lavesseur G, Autio H, Karpova N, et al. Impaired TrkB receptor signaling contributes to memory impairment in APP/PS1 mice. *Neurobiol Aging*. 2012;33:1122.e23–39.
65. Blazquez-Llorca L, Valero-Freitag S, Rodrigues EF, Merchán-Pérez Á, Rodríguez JR, Dorostkar MM, et al. High plasticity of axonal pathology in Alzheimer's disease mouse models. *Acta Neuropathol Commun*. 2017;5:14.
66. Wang Y, Ulland TK, Ulrich JD, Song W, Tzaferis JA, Hole JT, et al. TREM2-mediated early microglial response limits diffusion and toxicity of amyloid plaques. *J Exp Med*. 2016;213:667–75.
67. Zheng H, Jia L, Liu C-C, Rong Z, Zhong L, Yang L, et al. TREM2 promotes microglial survival by activating Wnt/ $\beta$ -catenin pathway. *J Neurosci*. 2017;37:1772–84.
68. Pickett EK, Herrmann AG, McQueen J, Abt K, Dando O, Tulloch J, et al. Amyloid Beta and Tau cooperate to cause reversible behavioral and transcriptional deficits in a model of Alzheimer's disease. *Cell Rep*. 2019;29:3592–3604.e5.
69. Sahara N, Lewis J, DeTure M, McGowan E, Dickson DW, Hutton M, et al. Assembly of tau in transgenic animals expressing P301L tau: alteration of phosphorylation and solubility. *J Neurochem*. 2002;83:1498–508.
70. Klionsky DJ, Abdalla FC, Abeliovich H, Abraham RT, Acevedo-Arozena A, Adeli K, et al. Guidelines for the use and interpretation of assays for monitoring autophagy. *Autophagy*. 2012;8(4):445–544.
71. Yoshii SR, Mizushima N. Monitoring and measuring autophagy. *Int J Mol Sci*. 2017;18(9):1865.
72. Inukai K, Funaki M, Ogihara T, Katagiri H, Kanda A, Anai M, et al. p85 $\alpha$  gene generates three isoforms of regulatory subunit for phosphatidylinositol 3-kinase (PI 3-kinase), p50 $\alpha$ , p55 $\alpha$ , and p85 $\alpha$ , with different PI 3-kinase activity elevating responses to insulin. *J Biol Chem*. 1997;272:7873–82.
73. Martiskainen H, Paldanius KMA, Natunen T, Takalo M, Marttinen M, Leskelä S, et al. DHCR24 exerts neuroprotection upon inflammation-induced neuronal death. *J Neuroinflammation*. 2017;14(1):215.
74. Peng Q, Malhotra S, Torchia JA, Kerr WG, Coggeshall KM, Humphrey MB. TREM2- and DAP12-dependent activation of PI3K requires DAP10 and is inhibited by SHIP1. *Sci Signal*. 2010;3(122):ra38.
75. Zou W, Reeve JL, Liu Y, Teitelbaum SL, Ross FP. DAP12 couples c-Fms activation to the osteoclast cytoskeleton by recruitment of Syk. *Mol Cell*. 2008;31:422–31.
76. Pruzin JJ, Nelson PT, Abner EL, Arvanitakis Z. Review: relationship of type 2 diabetes to human brain pathology. *Neuropathol Appl Neurobiol*. 2018;44(4):347–62.
77. Sweeney MD, Sagare AP, Zlokovic BV. Blood-brain barrier breakdown in Alzheimer disease and other neurodegenerative disorders. *Nat Rev Neurol*. 2018;14(3):133–50.
78. Montagne A, Nation DA, Sagare AP, Barisano G, Sweeney MD, Chakhoyan A, et al. APOE4 leads to blood-brain barrier dysfunction predicting cognitive decline. *Nature*. 2020;581:71–6.
79. Breslow JL. Mouse models of atherosclerosis. *Science* (80- ). 1996;272:685–8.

80. Bracko O, Vinarcsik LK, Cruz Hernández JC, Ruiz-Urbe NE, Haft-Javaherian M, Falkenhain K, et al. High fat diet worsens Alzheimer's disease-related behavioral abnormalities and neuropathology in APP/PS1 mice, but not by synergistically decreasing cerebral blood flow. *Sci Rep*. 2020;10(1):9884.
81. Leinonen V, Koivisto AM, Savolainen S, Rummukainen J, Tamminen JN, Tillgren T, et al. Amyloid and tau proteins in cortical brain biopsy and Alzheimer's disease. *Ann Neurol*. 2010;68:446–53.
82. Takalo M, Haapasalo A, Martiskainen H, Kurkinen KMA, Koivisto H, Miettinen P, et al. High-fat diet increases tau expression in the brain of T2DM and AD mice independently of peripheral metabolic status. *J Nutr Biochem*. 2014;25:634–41 Elsevier.
83. Velázquez KT, Enos RT, Bader JE, Sougiannis AT, Carson MS, Chatzistamou I, et al. Prolonged high-fat-diet feeding promotes non-alcoholic fatty liver disease and alters gut microbiota in mice. *World J Hepatol*. 2019;11:619–37.
84. Jeong J-H, Kang E-B. Effects of treadmill exercise on PI3K/AKT/GSK-3 $\beta$  pathway and tau protein in high-fat diet-fed rats. *J Exerc Nutr Biochem*. 2018;22:9–14.
85. Kang EB, Koo JH, Jang YC, Yang CH, Lee Y, Cosio-Lima LM, et al. Neuroprotective effects of endurance exercise against high-fat diet-induced hippocampal neuroinflammation. *J Neuroendocrinol*. 2016;28. <https://doi.org/10.1111/jne.12385>.
86. Luchsinger JA, Tang MX, Shea S, Mayeux R. Caloric intake and the risk of Alzheimer disease. *Arch Neurol*. 2002;59:1258–63.
87. Morris MC, Evans DA, Bienias JL, Tangney CC, Bennett DA, Aggarwal N, et al. Dietary fats and the risk of incident Alzheimer disease. *Arch Neurol*. 2003;60:194–200.
88. Moser VA, Pike CJ. Obesity accelerates Alzheimer-related pathology in APOE4 but not APOE3 mice. *eNeuro*. 2017;4. <https://doi.org/10.1523/ENEURO.0077-17.2017>.
89. Nam KN, Mounier A, Wolfe CM, Fitz NF, Carter AY, Castranio EL, et al. Effect of high fat diet on phenotype, brain transcriptome and lipidome in Alzheimer's model mice. *Sci Rep*. 2017;7(1):4307.
90. Graham LC, Harder JM, Soto I, De Vries WN, John SWM, Howell GR. Chronic consumption of a western diet induces robust glial activation in aging mice and in a mouse model of Alzheimer's disease. *Sci Rep*. 2016;6:21568.
91. Buccarello L, Grignaschi G, Di Giancamillo A, Domeneghini C, Melcangi RC, Borsello T. Neuroprotective effects of low fat-protein diet in the P301L mouse model of tauopathy. *Neuroscience*. 2017;354:208–20.
92. Minkeviciene R, Ihalainen J, Malm T, Matilainen O, Keksa-Goldsteine V, Goldsteins G, et al. Age-related decrease in stimulated glutamate release and vesicular glutamate transporters in APP/PS1 transgenic and wild-type mice. *J Neurochem*. 2008;105:584–94.
93. Salas IH, Weerasekera A, Ahmed T, Callaerts-Vegh Z, Himmelreich U, D'Hooge R, et al. High fat diet treatment impairs hippocampal long-term potentiation without alterations of the core neuropathological features of Alzheimer disease. *Neurobiol Dis*. 2018;113:82–96.
94. Etchecho M, Petrov D, Pedros I, Alva N, Carbonell T, Beas-Zarate C, et al. Evaluation of neuropathological effects of a high-fat diet in a presymptomatic Alzheimer's disease stage in APP/PS1 mice. *J Alzheimers Dis*. 2016;54:233–51.
95. Serrano-Pozo A, Frosch MP, Masliah E, Hyman BT. Neuropathological alterations in Alzheimer disease. *Cold Spring Harb Perspect Med*. 2011;1(1):a006189.
96. Moloney AM, Griffin RJ, Timmons S, O'Connor R, Ravid R, O'Neill C. Defects in IGF-1 receptor, insulin receptor and IRS-1/2 in Alzheimer's disease indicate possible resistance to IGF-1 and insulin signalling. *Neurobiol Aging*. 2010;31(2):224–43.
97. Liu Y, Liu F, Grundke-Iqbal I, Iqbal K, Gong C-X. Deficient brain insulin signalling pathway in Alzheimer's disease and diabetes. *J Pathol*. 2011;225:54–62 NIH Public Access.
98. Ho L, Qin W, Pompl PN, Xiang Z, Wang J, Zhao Z, et al. Diet-induced insulin resistance promotes amyloidosis in a transgenic mouse model of Alzheimer's disease. *FASEB J*. 2004;18:902–4.
99. Qin W, Zhao W, Ho L, Wang J, Walsh K, Gandy S, et al. Regulation of forkhead transcription factor FoxO3a contributes to calorie restriction-induced prevention of Alzheimer's disease-type amyloid neuropathology and spatial memory deterioration. *Ann N Y Acad Sci*. 2008;1147:335–47.
100. Bhat NR, Thirumangalakudi L. Increased tau phosphorylation and impaired brain insulin/IGF signaling in mice fed a high fat/high cholesterol diet. *J Alzheimers Dis*. 2013;36:781–9.
101. King D, Yeomanson D, Bryant HE. PI3King the lock: targeting the PI3K/Akt/mTOR pathway as a novel therapeutic strategy in neuroblastoma. *J Pediatr Hematol Oncol*. 2015;37(4):245–51.
102. Wullschlegler S, Loewith R, Hall MN. TOR signaling in growth and metabolism. *Cell*. 2006;124(3):471–84.
103. Dong W, Wang R, Ma LN, Xu BL, Zhang JS, Zhao ZW, et al. Autophagy involving age-related cognitive behavior and hippocampus injury is modulated by different caloric intake in mice. *Int J Clin Exp Med*. 2015;8:11843–53.
104. Portovedo M, Ignacio-Souza LM, Bombassaro B, Coope A, Reginato A, Razolli DS, et al. Saturated fatty acids modulate autophagy's proteins in the hypothalamus. *PLoS One*. 2015;10:e0119850.
105. Yamamoto T, Takabatake Y, Takahashi A, Kimura T, Namba T, Matsuda J, et al. High-fat diet-induced lysosomal dysfunction and impaired autophagic flux contribute to lipotoxicity in the kidney. *J Am Soc Nephrol*. 2017;28:1534–51.
106. Kim J, Kundu M, Viollet B, Guan KL. AMPK and mTOR regulate autophagy through direct phosphorylation of ULK1. *Nat Cell Biol*. 2011;13:132–41.
107. Arranz A, Doxaki C, Vergadi E, De La Torre YM, Vaporidi K, Lagoudaki ED, et al. Akt1 and Akt2 protein kinases differentially contribute to macrophage polarization. *Proc Natl Acad Sci U S A*. 2012;109:9517–22.
108. Jiménez C, Portela RA, Mellado M, Rodríguez-Frade JM, Collard J, Serrano A, et al. Role of the PI3K regulatory subunit in the control of actin organization and cell migration. *J Cell Biol*. 2000;151:249–61.
109. Luyendyk JP, Schabbauer GA, Tencati M, Holscher T, Pawlinski R, Mackman N. Genetic analysis of the role of the PI3K-Akt pathway in lipopolysaccharide-induced cytokine and tissue factor gene expression in monocytes/macrophages. *J Immunol*. 2008;180:4218–26.
110. Baufeld C, Osterloh A, Prokop S, Miller KR, Heppner FL. High-fat diet-induced brain region-specific phenotypic spectrum of CNS resident microglia. *Acta Neuropathol*. 2016;132:361–75.
111. Vinuesa A, Bentivegna M, Calfa G, Filipello F, Pomilio C, Bonaventura MM, et al. Early exposure to a high-fat diet impacts on hippocampal plasticity: implication of microglia-derived exosome-like extracellular vesicles. *Mol Neurobiol*. 2019;56:5075–94.
112. Park M, Yi JW, Kim EM, Yoon UJ, Lee EH, Lee HY, et al. Triggering receptor expressed on myeloid cells 2 (TREM2) promotes adipogenesis and diet-induced obesity. *Diabetes*. 2015;64:117–27.
113. Liu C, Li P, Li H, Wang S, Ding L, Wang H, et al. TREM2 regulates obesity-induced insulin resistance via adipose tissue remodeling in mice of high-fat feeding. *J Transl Med*. 2019;17(1):300.
114. Yuan P, Condello C, Keene CD, Wang Y, Bird TD, Paul SM, et al. TREM2 Haplodeficiency in mice and humans impairs the microglia barrier function leading to decreased amyloid compaction and severe axonal dystrophy. *Neuron*. 2016;90(4):724–39.
115. Hao S, Dey A, Yu X, Stranahan AM. Dietary obesity reversibly induces synaptic stripping by microglia and impairs hippocampal plasticity. *Brain Behav Immun*. 2016;51:230–9.
116. Walker JM, Dixit S, Saulsberry AC, May JM, Harrison FE. Reversal of high fat diet-induced obesity improves glucose tolerance, inflammatory response,  $\beta$ -amyloid accumulation and cognitive decline in the APP/PSEN1 mouse model of Alzheimer's disease. *Neurobiol Dis*. 2017;100:87–98.
117. McLean FH, Campbell FM, Sergi D, Grant C, Morris AC, Hay EA, et al. Early and reversible changes to the hippocampal proteome in mice on a high-fat diet. *Nutr Metab*. 2019;16:57.
118. Schlepckow K, Monroe KM, Kleinberger G, Cantuti-Castelvetri L, Parhizkar S, Xia D, et al. Enhancing protective microglial activities with a dual function TREM 2 antibody to the stalk region. *EMBO Mol Med*. 2020;12(4):e11227.
119. Wang S, Mustafa M, Yuede CM, Salazar SV, Kong P, Long H, et al. Anti-human TREM2 induces microglia proliferation and reduces pathology in an Alzheimer's disease model. *J Exp Med*. 2020;217(9):e20200785.
120. Valente T, Gella A, Fernández-Busquets X, Unzeta M, Durany N. Immunohistochemical analysis of human brain suggests pathological synergism of Alzheimer's disease and diabetes mellitus. *Neurobiol Dis*. 2010;37:67–76.
121. Prokop S, Miller KR, Labra SR, Pitkin RM, Hoxha K, Narasimhan S, et al. Impact of TREM2 risk variants on brain region-specific immune activation and plaque microenvironment in Alzheimer's disease patient brain samples. *Acta Neuropathol*. 2019;138:613–30.
122. Streit WJ, Braak H, Xue QS, Bechmann I. Dystrophic (senescent) rather than activated microglial cells are associated with tau pathology and likely precede neurodegeneration in Alzheimer's disease. *Acta Neuropathol*. 2009;118:475–85.

## Publisher's Note

Springer Nature remains neutral with regard to jurisdictional claims in published maps and institutional affiliations.